Wing shape evolution in bombycoid moths reveals two distinct strategies for maneuverable flight

Brett R. Aiello[a,b,c], Usama Bin Sikandar[d,e], Hajime Minoguchi[a], Katalina C. Kimball[b], Chris A. Hamilton[f], Akito Y. Kawahara[c,g,h], and Simon Sponberg[a,b]

[a]School of Physics, Georgia Institute of Technology, Atlanta, GA 30332, USA.; [b]School of Biological Sciences, Georgia Institute of Technology, Atlanta, GA 30332, USA.; [c]Florida Museum of Natural History, University of Florida, Gainesville, FL, 32611, USA.; [d]School of Electrical and Computer Engineering, Georgia Institute of Technology, Atlanta, GA 30332, USA.; [e]Department of Electrical Engineering, Information Technology University, Lahore, Pakistan; [f]Department of Entomology, Plant Pathology & Nematology, University of Idaho, Moscow, ID 83844, USA.; [g]Entomology and Nematology Department, University of Florida, Gainesville, FL, 32608, USA.; [h]Department of Biology, University of Florida, Gainesville, FL, 32611, USA.

A wide diversity of wing shapes has evolved, but how is aerodynamic strategy coupled to morphological variation? Here we examine how wing shape has evolved across a phylogenetic split between hawkmoths (Sphingidae) and wild silkmoths (Saturniidae), which have divergent life histories, but agile flight behaviors. Combined with kinematics of exemplar species, we find that these two diverse sister families have evolved two distinct strategies for agile flight. Each group has evolved distinct wing shapes in phylogenetic PCA-space. The notoriously agile hawkmoths have not evolved wing shapes typical of maneuverability, but rather ones that reduce power. Instead their kinematics favor maneuverability, primarily through higher wingbeat frequency. In contrast, silkmoths evolved maneuverable wing shapes and use kinematics that reduce power. Therefore, multiple strategies have evolved to achieve similar aerodynamic performance. We suggest flapping wings provide flexible aerodynamics through kinematics and might release morphological constraints, enabling the diversity of wing shapes across extant flyers.

wing shape | moth | flight | evolution | aerodynamics | maneuverability

INTRODUCTION

The functional demands associated with the behavioral repertoire of a species can drive the evolution of locomotor morphology and appendage movement. The wings are a prominent and morphologically diverse features of flying animals (Wootton, 1992; Le Roy et al., 2019), which impact moments of inertia and aerodynamics (Dudley, 2000). Wing shape varies across many groups of flying organisms, but unlike fixed wings, flapping wing aerodynamics also depend on active wing movement. These multiple factors make it challenging to link evolutionary patterns of wing shape to the larger strategies of aerodynamic performance employed by animals or to translate these patterns to engineered flapping wing design.

The wing shape of insects, the most speciose clade of extant animals, likely faces strong selective pressures to meet the functional demands of a species (Wootton, 1992). Many flying vertebrates can "morph" wing shape to modulate aerodynamic forces (Lentink et al., 2007; Crandell and Tobalske, 2011; Riskin et al., 2010; Stowers et al., 2017; Baliga et al., 2019). Flexible shapes may reduce selective pressure on wing morphology. Insects do not contain intrinsic wing musculature and cannot morph wing shape, except

through actuation at the hinge. However, interspecific kinematic flexibility does exist across insects, and insects employ a diversity of kinematics (Dudley, 2000). Further, alteration of the expression pattern of a single gene in *Drosophila melanogaster* can advantageously modify wing shape to significantly enhance aerodynamic agility (Ray et al., 2016), suggesting a strong genotype to phenotype link in wing shape on which selection can act. While the aerodynamics of flight can be altered through the modification of wing shape, size, and movement (kinematics), how these traits evolve within insect clades, whether distinct evolutionary groups adopt consistent flight strategies for, and how evolutionary shifts in wing shape and kinematics impact aerodynamic performance remains unclear.

Certain features of wing shape have known aerodynamic consequences for maneuverability, force production, and power, most notably: 1) wing loading, $W_s = S/m_t$, where S is the wing area and m_t is the total body mass, 2) wing aspect ratio, AR, AR $= R^2/S$, where R is wing span length, and 3) the distribution of area along the long axis of a wing (radius of the second moment of area, $\hat{r}_2$). A decrease in W_s, absent other changes, increases maneuverability. W_s is proportional to turning radius in birds (Burns and Ydenberg, 2002; Hedenstrom and Rosen, 2001), bats (Aldridge, 1987; Norberg and Rayner, 1987), and Lepidoptera (Betts and Wootton, 1988) and inversely related to rotational speeds and accelerations during maneuvers in birds (Hedenstrom and Rosen, 2001; Dakin et al., 2018) and Lepidoptera (Betts and Wootton, 1988; Berwaerts et al., 2002). W_s is also positively correlated with flight speed in both vertebrates (Norberg and Rayner, 1987) and insects (Betts and Wootton, 1988; Dudley and Srygley, 1994; Dudley, 2002). A reduction in AR increases both power requirements and maneuverability, typically through a reduction in wing moment of inertia as seen in butterflies (Betts and Wootton, 1988; Cespedes et al., 2015; DeVries et al., 2010). High AR reduces the power requirements of flight by reducing induced drag from wing tip vortices (Norberg and Rayner, 1987; Pennycuick, 1968). An increase in $\hat{r}_2$ can decrease maneuverability through an increase in the moment of inertia of the wing as more wing area, and likely mass, is distributed more distally along the wing in comparison to a wing of a lower $\hat{r}_2$.

Although AR, W_s, and $\hat{r}_2$ are often used to infer performance, these relationships between wing shape and performance assume that other factors remain constant; performance might depend as much on differences in wing kinematics as on wing shape. For example, rotational maneuverability can be enhanced by increasing wing beat frequency, n, which increases active torque generation (Hedrick et al., 2009). Indeed, n increases during maneuvers in hovering hawkmoths (Cheng et al., 2011) and hummingbirds (Cheng et al., 2016b). The power requirements of flight are also dependent on wing movement. While it is possible for insects to produce the same flight behavior through different sets of kinematics (Hedrick and Daniel, 2006), insects employ kinematics that minimize energy consumption (Berman and Wang, 2007). Therefore, concomitant changes in wing kinematics may produce very different aerodynamic implications for wing shape.

The moth superfamily Bombycoidea, provides a prime opportunity to test how wing shape evolves in a closely related species within a diverse clade of more than 5,000 species (Kitching et al., 2018; Lemaire and Minet, 1998). Within Bombycoidea, the sister families Sphingidae and Saturniidae (Breinholt et al., 2018; Kawahara et al., 2019; Hamilton et al., 2019), have ∼1600 and ∼3400 described species respectively (Kitching et al., 2018). These two families display an extraordinary diversity of wing shape, and strikingly divergent life history strategies (Tammaru and Haukioja, 1996) and flight behaviors. Within Sphingidae (hawkmoths), *Manduca sexta*, and more recently *Daphnis nerii*, *Hyles lineata*, and *Macroglossum stellatarum*, are models for studies on flight control (Sponberg et al., 2015; Willmott and Ellington, 1997a; Natesan et al., 2019), vision (Windsor et al., 2014; Stöckl et al., 2017b), olfaction (Hildebrand, 1996; Gage et al., 2013; Riffell et al., 2013), and multisensory integration (Roth et al., 2016). Hawkmoths are most known for their ability to sustain long duration bouts of hovering while feeding from flowers (Wasserthal, 1993; Farina et al., 1994; Sprayberry and Daniel, 2007; Sponberg et al., 2015). In addition to the evolution of the hovering behavior, hawkmoths are often described as active, fast-flying, and maneuverable (Callahan, 1965; Tuttle, 2007). Some hawkmoths can successfully track flowers oscillating up to frequencies of 14 Hz (Sponberg et al., 2015; Stöckl et al., 2017a), suggesting a high degree of maneuverability. Saturniidae (wild silkmoths) is one model group for studying the predator-prey arms race (Barber et al., 2015; Kawahara and Barber, 2015; Rubin et al., 2018). Many silkmoth species display a flight behavior often described as bobbing, but can also be fast and agile when escaping from predators (Jacobs and Bastian, 2016; Janzen, 1984; Lewis et al., 1993). Silkmoths lack functional mouth parts and must rely on the strictly finite energy stores, gathered during the larval period, during their entire reproductive adult life stage (Tuskes et al., 1996).

Here we use the wing diversity and life history differences between the sister families, Sphingidae and Saturniidae, to test if they adopt distinct flight strategies with correspondingly distinct wing shapes. First, we use museum specimens to explore how wing shape varies in an explicitly phylogenetic context across a diverse group of agile flying insects. We test the hypothesis that wing morphology diverged on two distinct trajectories when hawkmoths and silkmoths split. Alternatively, differences in wing shape and size might arise more within each group, driven by the demands of individual species.

We next consider measures of wing morphology (AR, W_s, and $\hat{r}_2$) across Bombycoidea to test if the two groups have shapes associated with maneuverable flight. Given their flight performance and maneuverability, we hypothesize that both groups evolved forewings of low AR, W_s, and $\hat{r}_2$. Alternatively, because most hawkmoths (possible exception of the Ambulycini tribe) require high power output in order to sustain long bouts of hovering while feeding and because adult stage silkmoths do not feed, we hypothesize that both groups have evolved wing shapes that reduce power requirements by increasing wing AR or length or that

the two groups diverge for separate strategies.

Finally, to assess the potentially subtle interplay of shape, size, and kinematics, we quantified three-dimensional wing kinematics during forward flight from live specimens of two species representing the wing shapes of each family. We estimated quasi-steady aerodynamic force production and power requirements using a blade element model (Sane and Dickinson, 2002; Faruque and Humbert, 2010b; Cheng et al., 2016a; Han et al., 2015). Using these two species, we can place the broader differences in wing shape into the context of kinematic differences for these particular species. Determining whether major transitions in flight strategy occur through changes in wing shape, kinematics, or their combination will broadly inform the evolution of animal flight and our ability to infer aerodynamic consequences from wing shape alone.

MATERIALS AND METHODS

Phylogenetics. In order to understand the evolution of wing shape across the Bombycoidea, we sampled representatives of all Bombycoidea families. In total, the phylogenetic dataset included 57 species and one outgroup – the Lasiocampidae, the sister lineage to the Bombycoidea. Sampling was highest in the Saturniidae (25 sp.) and Sphingidae (24 sp.). Sequences were a mixture of previously sequenced individuals from prior studies (Breinholt et al., 2018; Rubin et al., 2018) and novel specimens (see Table S1). AHE sequences represented 53 species, while four species had their AHE loci mined from transcriptomic data (Table S1). Nineteen species were newly sequenced for this project, while 38 came from previously published datasets (Table S1). Species were chosen in order to capture the majority of the wing shape diversity throughout the Sphingidae and Saturniidae, based on availability in the collections at the Florida Museum of Natural History, Gainesville, FL, USA (FLMNH).

Specimens were obtained from historically preserved dry collections and molecular tissue collections stored at the Florida Museum of Natural History. DNA extraction from pinned museum specimens followed the protocol outlined in (Hamilton et al., 2019). Field-collected specimens were stored in $\geq 95\%$ ethanol, RNAlater (Sigma Aldrich, Saint Louis, MO, United States), or papered and dried with silica gel. Genomic DNA was extracted using OmniPrep Genomic DNA Extraction Kits (G-Biosciences, St. Louis, MO, USA) and DNeasy Blood and Tissue Kits (Qiagen, Valencia, CA, USA). DNA concentration was evaluated through agarose gel electrophoresis and fluorometry using a Qubit 2.0 (Invitrogen, Thermo Fisher Scientific, Carlsbad, CA, USA).

We used the Bombycoidea-specific 'BOM1' Anchored Hybrid Enrichment (AHE) probe set to target 571 loci (Hamilton et al., 2019). AHE is a targeted-sequencing methodology designed to capture hundreds of unique orthologous loci (i.e., single copy, phylogenetically-informative markers) from across the genome, for resolving both shallow and deep-level evolutionary relationships (Lemmon et al., 2012; Breinholt et al.,

2018).

Library preparation, hybridization enrichment, and Illumina HiSeq 2500 sequencing (PE100) was carried out at RAPiD Genomics (Gainesville, FL, USA). Specimen wing vouchering and tissue storage methods follow (Cho et al., 2016). All DNA extracts and specimens preserved in ethanol, RNAlater, or those freshly papered were stored at $-80°$ C at the FLMNH, McGuire Center of Lepidoptera and Biodiversity (MGCL). Historically preserved dry collection specimens were kept in their traditional storage method - pinned in their tray or papered in a box, at the MGCL.

The bioinformatics pipeline of (Breinholt et al., 2018) was used to clean and assemble raw Illumina reads for each AHE locus. The pipeline uses a probe-baited iterative assembly that extends beyond the probe region, checks for quality and cross contamination due to barcode leakage, removes paralogs, and returns a set of aligned orthologs for each locus and taxon of interest. To accomplish these tasks, the pipeline uses the Bombyx mori genome (Xia et al., 2004), and the BOM1 AHE reference library. Previously published scripts (Breinholt et al., 2018) and instructions (Hamilton et al., 2019) on the pipeline are available in Dryad (https://doi.org/10.5061/dryad.5df18fp).

Loci for phylogenetic analysis were selected by applying a cutoff of $\geq$60% sampled taxa recovery (i.e., for a locus to be included in the analysis, the locus had to be recovered in at least 60% of the sampled taxa). The pipeline evaluates density and entropy at each site of a nucleotide sequence alignment. We elected to trim with entropy and density cutoffs only in flanking regions, allowing the probe region (exon) to be converted into amino acid sequences. For a site (outside of the probe region) to remain, that site must then also pass a 60% density and 1.5 entropy (saturation) cutoff, rejecting sites that fail these requirements. A higher first value (60) increases the coverage cutoff (e.g., a site is kept if 60% of all taxa are represented at that site). A higher second value (1.5) increases the entropy cutoff (i.e., entropy values represent the amount of saturation at a site); sites with values higher than 1.5 possess higher saturation and are thus deleted). Following (Hamilton et al., 2019), we built and utilized a Pr+Fl dataset; a concatenated dataset consisting of 605 probe regions + a flanking supermatrix for phylogeny inference. The final dataset comprised 606 loci and 222,369 bp.

AliView v1.18 (Larsson, 2014) was used to translate the nucleotides to amino acids, check for frame shifts, and edit sequencing errors or lone/dubious indels. Because flanking sequences are generally non-coding and sites have been deemed homologous, the flanking sequences (i.e., those before and after the probe regions), were separated from the exons, then combined and treated together as an independent partition. Due to the filtering steps in the bioinformatics pipeline (i.e., site orthology, and density and saturation evaluation), the flanking partition can be viewed as a SNP supermatrix, where each site is homologous and independent, but uninformative sites, saturated sites, or sites with large amounts missing data removed.

Specimens whose AHE loci were mined from transcriptomes did not have flanking data due to the nature of transcriptomic data.

A concatenated supermatrix was assembled using FASconCAT-G v1.02 (Kueck and Longo, 2014). Phylogenetic inference was performed in a maximum likelihood (ML) framework using IQ-TREE v1.5.3 (Nguyen et al., 2015). Within this framework we searched for the most appropriate model of nucleotide substitution, as well as 1000 random addition sequence (RAS) replicates, and 1000 replicates each for both ultrafast bootstraps (UFBS) and SH-aLRT tests to find the "best" tree and node support. We classified nodes as well-supported if they were recovered with support values of UFBS $\geq$95 and SH-aLRT $\geq$80 (Minh et al., 2013; Nguyen et al., 2015). All branch length estimates are in units of substitutions per site. In the ultrametric tree used for analyses, the branch lengths were scaled relative to each other. All pipeline steps and phylogenomic analyses were conducted on the University of Florida HiPerGator HPC (http://www.hpc.ufl.edu/). All alignment FASTA files, partition files, tree files, and other essential data files used for phylogenetic inference are available as supplementary materials on Dryad.

Museum Specimen Imaging. Moth specimens from the collections at the FLMNH were imaged using a 60mm lens (Canon, Tokyo, Japan) mounted to a Canon EOS 7D camera (Canon, Tokyo, Japan). At least one individual of each of the 57 species was imaged. See Table S1 for details on the number and sex of specimens imaged per species. For this analysis, male specimens were analyzed when available (53 of 57 species). We chose to focus on males because they are known to exhibit higher flight activity in comparison to females (Gilchrist, 1990; Le Roy et al., 2019).

Body and Wing Measurements and Morphometrics. The body and wing morphology was digitized from museum images using the StereoMorph package (version 1.6.2) (Olsen and Westneat, 2015) in R (version 3.4.2; The R Foundation for Statistical Computing). Eight landmarks were digitized to characterize body size and shape (Fig. 1A). The rostral and caudal bases of both the forewing and hindwing were also digitized. Finally, a series of third order Bezier curves were used to outline the right forewing (Fig. 1A). The curves were then resampled using the StereoMorph package to generate 50 evenly spaced points (semilandmarks) around the wing perimeter. For species with multiple individuals, each wing was aligned at the rostral base of the wing and forewing shape was averaged to produce a mean set of 50 semilandmarks to be used in further analysis. Similarly, for species with multiple individuals, the length and width of each body segment (head, thorax, and abdomen) were averaged to obtain mean values for each species.

The digitized output of each moth was further analyzed in MATLAB (version R2018b - 9.5.0.944444). Body mass was estimated by modeling the body as three ellipsoids: one for the head, thorax, and abdomen. The length and width of each body segment were measured as the distance between the minimum and

maximum value for that segment. The width of the head was assumed to be equal to its length. The dorso-ventral depth of every segment was assumed to be equal to its width. The density of each body segment was assumed to be equal to water (Ellington, 1984a).

Forewing measurements began by rotating each forewing so its long axis was perpendicular to the long axis of the body. Wing length (R) was measured as the distance between the minimum and maximum value of the wing outline. All additional wing parameters (AR, W_s, and r_2) were calculated following (Ellington, 1984a). The wing was assumed to have a thickness equal to 0.5% mean chord length and a density equal to water. The wing area was then filled with equally distributed points that were each assigned an equal mass fraction. Wing beat frequency (n) was estimated using an equation derived through dimensional analysis of insect body mass and wing area (Table A.1; (Deakin, 2010)). Finally, body mass specific mean inertial power of the wings (P_{acc}) was calculated (see Table A.1) following published methods (Ellington, 1984c). Stroke amplitude was not available for every species so the same half stroke amplitude of 60° was used across all species. The potential impact of different kinematics is discussed in the comparison of the exemplar species from which kinematics were obtained.

To examine the variation in forewing shape while accounting for phylogeny, we conducted a phylogenetic principal components analysis (pPCA) (Revell, 2009). A pPCA finds the dimensions of wing shape that maximize the covariance of the component shape variables, but corrects the covariance with a relatedness matrix that takes into account the shared evolutionary history of the samples. For each species, the mean forewing semilandmarks were aligned by Procrustes superimposition to obtain size and orientation corrected Procrustes coordinates (implemented with gpagen function in Geomorph R package (version 3.1.2)). Next, the pPCA was conducted on the Procrustes coordinates for each species (implemented with the phyl.pca function in the R package Phytools (version: 0.6-60) (Revell, 2012)). We then projected wing shape back on to the first four pPC axes (Olsen, 2017). To test if clades were significantly clustered in four dimensional pPC morphospace, we conducted a MANOVA where the pPC scores of pPC1, 2, 3 and 4 were used as the response variable and clade (hawkmoths, silkmoths, or ancient bombycoid lineages) was the factor. Additionally, we tested for phylogenetic signal in each wing shape variable across the full phylogeny and within each subclade (hawkmoths, silkmoths, and the clade comprising the hawkmoth-silkmoth sister families). These analyses were conducted in RStudio (version 1.1.383; RStudio, Inc., Boston, MA).

Ancestral State Reconstruction. Ancestral state reconstructions were conducted to determine the evolutionary history of each wing trait as well as the wing shape PC scores. Maximum likelihood ancestral state reconstructions (fastAnc in phytools R package (version 0.6.60) (Revell, 2012)) used a Brownian motion model of evolution and estimates the maximum likelihood state estimations for all internal nodes by rerooting the phylogeny at each internal node and computing the contrasts state at the root according to

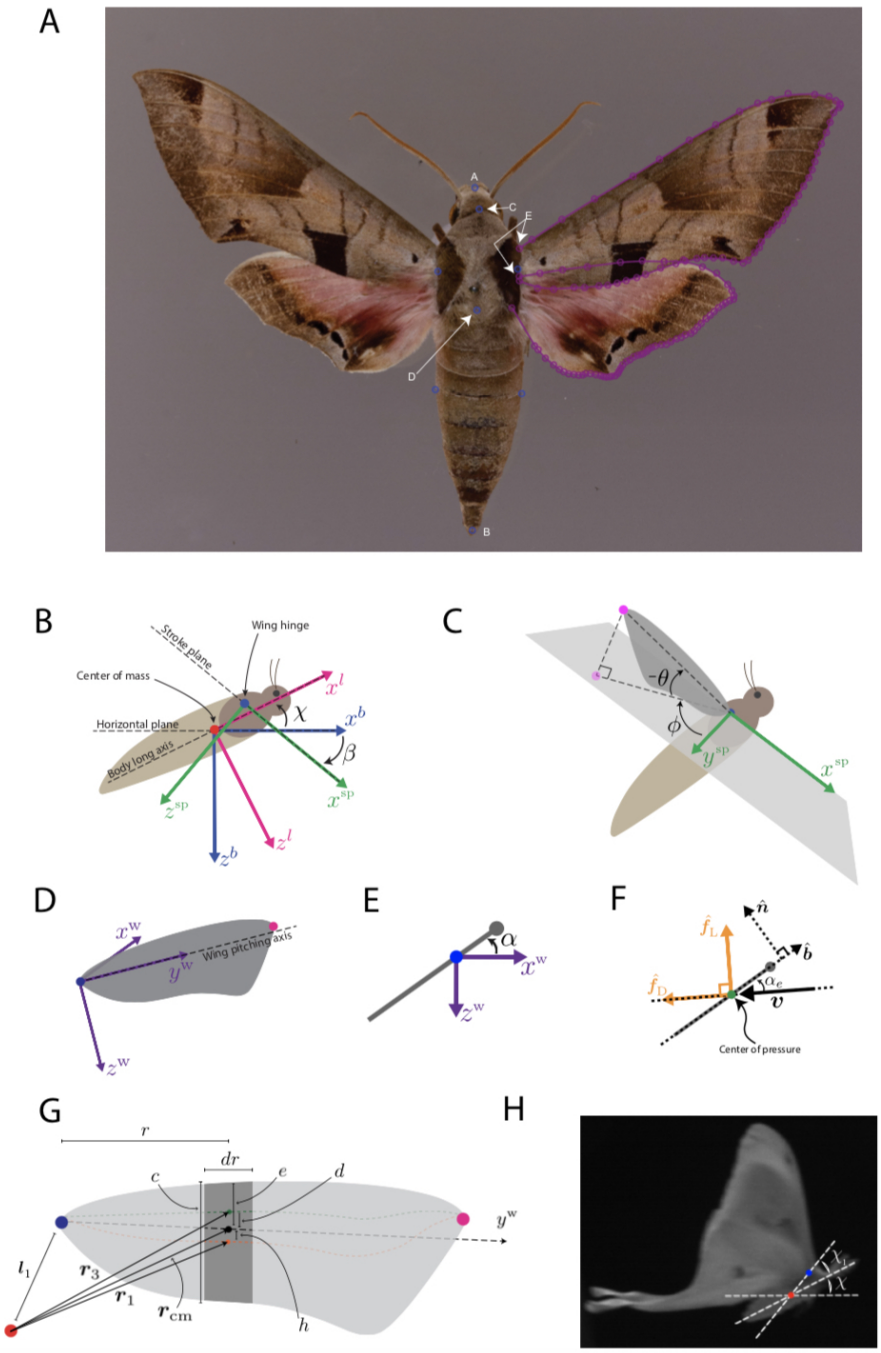

Fig. 1. **A** Summary of body landmarks and coordinate systems. Eight landmarks (blue points) capture body size and wing attachment. Sagittal landmarks were placed at the tip of the head (1), caudal tip of the abdomen (2), junction between the head and thorax (3), and junction between the thorax and abdomen (4). Parasagittal landmarks were placed at the widest points of the thorax and abdomen and the rostral and caudal base of the forewing (5) and hindwing. Each wing was outlined using a series of Bezier curves (purple points). Each curve was free to vary in perimeter length, and, typically, more points were used to generate the outline around more complex regions of the wing (see distal tip versus leading edge). **B** The body-attached coordinate frame (blue), the body-long coordinate frame (pink) and the stroke-plane frame (green). The red dot represents the location of the center of mass and the blue dot represented the wing hinge. β is the stroke-plane angle and χ is the body angle. **C** Definitions of wing kinematic angles: ϕ and θ defined with respect to the stroke-plane. **D**-**E** The wing-attached coordinate frame and wing-pitching angle α. **F** Relative airflow, effective angle of attack, and lift and drag components of the translational aerodynamic force. **G** Various length parameters relevant to a single wing strip. Red, blue, and pink circles correspond to the body center of mass, wing hinge, and wing tip. Dashed green, orange, and black lines are the quarter-chord, half-chord, and wing pitching axis, respectively. **H** Inclination angle of the wing-hinge point (blue) from the center of mass (red).

the contrasts algorithm (Felsenstein, 1985).

Live specimens. Live specimens were obtained as pupae from a breeder for two species: *Actias luna* (Saturniidae) and *Eumorpha achemon* (Sphingidae). These two species were chosen because they were readily available in large numbers and were also widely separated in pPCA morphospace, providing a general representative from each family. Caterpillars of each species were acquired by collecting eggs from local adult moths, and all caterpillars were reared on species-specific host plants. Pupae were stored in an incubator (Darwin Chambers, model: IN034LTDMMP, Saint Louis, MO) set to a temperature of 23° C and a relative humidity of 65%.

Three-dimensional Kinematics. Moths were transferred to the wind tunnel in individual containers with a moist tissue to prevent desiccation. Each individual was dark adapted at the wind tunnel for 1hr prior to the start of filming. Flight experiments were conducted in a 100×60.96 working section of an open-circuit Eiffel-type wind tunnel (ELD, Inc, Lake City, MN). The stream-wise turbulence of the wind tunnel does not exceed 0.5% and the flow speed did not vary by more than 2%. For a detailed overview of the specifications of the wind tunnel see (Matthews and Sponberg, 2018).

Moths were enticed to fly by providing a mild wind speed of 0.7 ms^{-1}. Flight bouts were filmed at 2000 frames s^{-1} for *E. achemon* and 1000 frames s^{-1} for *A. luna* using three synchronized Photron high-speed digital video cameras (Mini UX 100; Photron, San Diego, CA, USA) at a resolution of 1280×1024. Two cameras (one upwind and one downwind) were positioned below the wind tunnel test section at a 45° angle relative to the direction of flow. A third camera was placed laterally and orthogonal to plane of the first two cameras. The working section of the wind tunnel was illuminated with six 850Nm IR light (Larson Electronics, Kemp, TX, USA) and a neutral density filter, white LED "moon" light (Neewer CW-126) to control illumination conditions. Videos were digitized and calibrated in XMALab (Knorlein et al., 2016). From the exported 3D points we characterized the wing kinematics by calculating the following variables (Figs. 1 B-E): wing beat frequency (n), stroke plane angle (β), sweep angle (ϕ), deviation angle (θ), and feathering angle (α). The definition of each angle follows those outlined in (Willmott and Ellington, 1997a).

Extracting the 3D Time-series Data. We extracted the time series data of 3D coordinates of seven landmark points on a moth's body in the lab frame: head, thorax, abdomen, left wing hinge, right wing hinge, right wing tip and a point on the trailing edge of the forewing. We tracked the coordinates of head, thorax and abdomen to estimate the orientation of the body; and the points on the right wing hinge, right wing tip and trailing edge to estimate the wing kinematics. In videos, we only extracted data from forward flight bouts. From each individual, we digitized 1 complete wingstroke that was contained within a larger set of wingstrokes during forward flight. We never digitized the first or final wingstroke from a forward flight

bout. For each wing stroke, at minimum, every other frame was digitized, and, in most videos, we digitized every frame. To specify the body coordinate system, we defined the absolute horizontal plane using the lateral camera view. Using the horizontal plane, we defined the absolute vertical vector, i.e. the direction of the force of gravity.

Body Coordinate Frames. We defined a body-attached frame to specify the direction of motion, and a body-long frame to keep track of the orientation of the moth's body as shown in Fig. 1B. These frames share a common origin located at the center of mass. The body-long positive x-axis, x^l, points from the center of mass towards the center of head; the z^l-axis is perpendicular to x^l dorsally and lies in a vertical plane that splits the moth's body into symmetric halves; the y^l-axis is the cross product of z^l and x^l according to the right-handed coordinate system. The body-attached positive x-axis, x^{b}, starts from the center of mass and points in a direction that is the projection of x^l-axis on the absolute horizontal plane; z^{b} points towards the direction of gravity; y^{b} is the cross product of z^{b} and x^{b}. This makes the $x^{\mathrm{b}}y^{\mathrm{b}}$-plane the absolute horizontal plane irrespective of moth's body orientation.

Stroke-plane Coordinate Frame of the Right Wing. We used the definition of stroke-plane in (Willmott and Ellington, 1997a) to estimate the stroke-plane for each wing stroke and then attached a coordinate frame. The origin of a stroke-plane frame is at the wing hinge point as shown in Fig. 1B . Anatomically, we defined the wing hinge point as a single point located at one-third the distance from the rostral to the caudal wing hinge. For the right wing, the positive x^{sp}-axis is in the direction of the downstroke and lies within the x^{b}-z^{b} plane; y^{sp} is outward from the right wing hinge parallel to the y^l-axis in a direction from the left wing hinge to the right wing hinge; and z^{sp} is the cross-product of x^{sp} and y^{sp}.

Wing-attached Coordinate Frame of the Right Wing. To calculate the forces on the wing at each time instance, a coordinate frame attached to the wing is required. Our choice of such a coordinate frame is shown in Fig. 1D. The origin of this wing-attached frame is also at the wing hinge point. The y-axis of the wing-attached coordinate frame, y^{w}, is the anatomical wing-pitching axis of the moth, which was set to be perpendicular to the body-long axis and lied in the same plane as the forewing. The wing-attached coordinate frame is obtained by sequentially rotating the stroke-plane frame through wing kinematic angles ϕ and θ about the current z- and x-axis respectively. Hence, the wing-attached frame rotates with the ϕ and θ rotations of the wing. This means that when both ϕ and θ are equal to zero, the stroke-plane and wing-attached coordinate frames are perfectly aligned. For simplicity, our model's wing-attached frame does not rotate with the wing's pitching motion (α).

Right Wing Kinematics. The 3D time-series data of the trajectories were linearly interpolated for any frame that was not digitized and then smoothed using a moving-average filter with a window length of 10 frames. Next, we transformed the data from the camera-calibrated frame to the wing-attached frame and split the data into wing strokes starting at a wingtip position that can be kept consistent across different wing strokes. The series of transformations we applied simplified the extraction of the time series data of individual wing strokes from the start of a downstroke to the end of the subsequent upstroke. We applied a series of transformations to transform the data from the camera-calibrated frame to the wing-attached frame and then split the data. The origin was shifted to the right wing hinge through a translation. This allowed the movement of the wing tip to be restricted to just the rotations.

The stroke plane was defined for each wing stroke using a best-fit line through the 3D wing tip trajectory and relied on the vector between the left and right wing hinges. The stroke plane was fit to each wing stroke separately. Next, we calculate the two angles of the wing kinematics: the wing sweep angle (ϕ) and the deviation angle (θ) with respect to the wing-stroke, as defined in Fig. 1C. These angles are basically the azimuth and elevation angles, respectively, of the wing tip with respect to the stroke-plane frame following the definitions in (Willmott and Ellington, 1997a). However, we introduced a sign flip to the deviation angle θ to specify it as a (positive) rotation about our x^{w}-axis.

Next, we calculated the wing pitching (feathering) angle α is shown in Fig. 1E, which is the angle of rotation of the wing about the y^{w}-axis. We found this angle by first numerically aligning the wing's surface-plane with the stroke-plane and then calculating the angle between the two planes. The wing's surface-plane was specified by two points tracked on the forewing and the third point at the wing hinge. The alignment was performed by reversing the θ (stroke deviation) rotation at each time instance. The stroke-plane angle β for each wingstroke was calculated as the smaller angle between the stroke-plane and the x^{b}-y^{b} plane, assuming that during one wingstroke the stroke plane did not rotate with respect to the body-attached frame. The body angle specifies the pitch orientation of the body-long coordinate frame with respect to the body-attached frame. The body angle χ for each wing stroke was calculated as the smaller angle between the wing stroke-averaged x^{l}-axis and the x^{b}-y^{b} plane.

Fitting a Fourier Series to the Wing Kinematics. In total, we extracted right wing kinematics from three individual moths of both species for a total of three wing strokes from *E. achemon* and three wing strokes from *A. luna*. For each species, we first time-scaled the wing kinematics data from the three wing strokes to their mean time period and calculated the mean ϕ, θ and α. We then, for each species, fit the following

third order Fourier series to the species averaged wing kinematic angles:

$$\phi(t) = a_{\phi,0} + \sum_{k=1}^{3} a_{\phi,k}\cos(2\pi knt) + b_{\phi,k}\sin(2\pi knt), \quad [1]$$

$$\theta(t) = a_{\theta,0} + \sum_{k=1}^{3} a_{\theta,k}\cos(2\pi knt) + b_{\theta,k}\sin(2\pi knt), \quad [2]$$

$$\alpha(t) = a_{\alpha,0} + \sum_{k=1}^{3} a_{\alpha,k}\cos(2\pi knt) + b_{\alpha,k}\sin(2\pi knt), \quad [3]$$

where n is the wingbeat frequency and $a_{\phi,k}, a_{\theta,k}, a_{\alpha,k}, b_{\phi,k}, b_{\theta,k}, b_{\alpha,k}$ are the Fourier series coefficients. The values of the Fourier coefficients are summarized in Table 2 and the graphs of the Fourier-fitted wing kinematics are shown in Fig. 4.

The blade element model. A blade element model was used to evaluate the quasi-steady aerodynamic forces produced during flapping flight for two species: *A. luna* and *E. achemon* (details in the next section). Briefly, the model estimated the contribution of translational, rotational, and added mass to the total aerodynamic force (Sane and Dickinson, 2001, 2002; Faruque and Humbert, 2010a,b; Han et al., 2015; Kim et al., 2015; Cheng et al., 2016a). Although the main focus of this manuscript is on the forewing, to ensure accurate comparisons of aerodynamic forces during flight between these two species, we used the total wing area and shape generated by the overlapping forewing and hindwing as the wing shape in our blade element model. The wing size and shape used for each species was the mean wing size and shape calculated from the museum specimens used in this study. Several configurations of the model were used to assess the relative contribution of wing shape, size, kinematics and flight speed to aerodynamic force production. The specific kinematic and flight speed variables input to each model are outlined in the results. In the base model, Model 1, stroke plane angle and flight velocity (horizontal and vertical) parameters are set equal to that of the species mean obtained from the three-dimensional kinematic analysis. In Model 1, the wing kinematics are those of a third order Fourier series fit to the mean kinematics (three wing strokes from three individuals) of each species.

The blade-element model for forward flight includes the effects due to the steady translational motion of the wing as well as some of the unsteady nature of translation (leading edge vortex, for example) and rotation of the wing (Ellington et al., 1996; Hedrick and Daniel, 2006; Kim and Han, 2014). Some of these unsteady effects can be captured by using empirically measured lift and drag coefficients, in addition to considering the effect of force due to the added mass of the air around the airfoil (Han et al., 2015; Usherwood and Ellington, 2002). Therefore, in our model, we assumed the total aerodynamic force as the sum of the translation, rotational, and added mass forces and used empirical coefficients of lift and drag taken from a robotic flapper using dynamically scaled kinematics from the hawkmoth *Manduca sexta* (Han et al., 2015).

First, we provide a summary of the overall approach and then detail the specific formulation of each

step in the blade element model in subsequent sections. All symbols the mathematical notation used in the model are defined in Table A.1. We started by considering the wing of each species as a thin, rigid plate. As is standard in blade element models, we divided the wing into 200 chord-wise strips so that each strip could be treated as an airfoil. To calculate the aerodynamic forces on a strip, we next determined airflow velocity relative to the wing. For this, we modeled the wing motion according to the measured wing kinematics: sweep, deviation and pitching motion relative to a stroke plane inclined at a constant angle. We also consider the contribution of the body translational and rotational velocities to the overall relative airflow velocity, as in previous models (Faruque and Humbert, 2010a; Cheng et al., 2016a). This causes each blade element to have its own relative airflow velocity and effective angle of attack. We calculated the translational and rotational aerodynamic force of each blade element following (Ellington, 1984b; Kim and Han, 2014; Cheng et al., 2016a). We calculated the added-mass force in a non-inertial frame following (Maybury and Lehmann, 2004; Sane and Dickinson, 2001), which considers both the translational and rotational acceleration of the wing as well as the non-inertial nature of the wing-attached frame. We calculated all the aerodynamic forces in a coordinate frame attached to the wing and then summed over all the strips to calculate the total force on the wing. We also calculated aerodynamic moments using moment arms that assume translational force acting at a quarter-chord distance from the leading edge while the rotational and added-mass forces act at a half-chord distance (Ellington, 1984b; Han et al., 2015; Truong et al., 2011). Then we transformed aerodynamic forces and moments to the body-attached frame, which is an inertial frame if the moth is flying at a constant velocity with no body rotations. In the end, we calculated induced power for further comparison of the flight performance of the two species.

Relative Airflow Velocity. We defined relative airflow velocity $\boldsymbol{v}$ of a small blade element strip as the velocity of the airflow relative to the strip. This relative airflow is caused by the overall motion of the strip relative to the surrounding air due to its rotation about the wing hinge, body translation and rotation, and possibly wind.

$$\boldsymbol{v}^{\mathrm{w}} = -\left(\boldsymbol{v}_{\mathrm{b}}^{\mathrm{w}} + \boldsymbol{\omega}_{\mathrm{b}}^{\mathrm{w}} \times \boldsymbol{r}_{\mathrm{cm}}^{\mathrm{w}} + \begin{bmatrix} -r\dot{\phi} \\ 0 \\ r\dot{\theta} \end{bmatrix}\right) \quad [4]$$

where $\boldsymbol{v}_{\mathrm{b}}^{\mathrm{w}}$ is the body velocity relative to the wind but measured in the wing-attached frame, $\boldsymbol{\omega}_{\mathrm{b}}^{\mathrm{w}}$ is the body angular velocity pseudovector in the wing-attached coordinate frame, $\boldsymbol{r}_{\mathrm{cm}}^{\mathrm{w}}$ is the vector from the body center of mass to the center of the strip, r is the distance from wing hinge to the vertical mid-chord line of the strip (see Fig. 1G), and $\dot{\phi}$ and $\dot{\theta}$ are the stroke positional (sweep) and stroke deviation angular velocities of the wing, respectively. For the calculations performed on the data relevant to this paper, there were no body rotations so $\boldsymbol{\omega}_{\mathrm{b}}^{\mathrm{w}}$ was equal to zero.

The Effective Angle of Attack. The effective angle of attack of the strip is defined as the angle between the chord line vector from leading edge to the trailing edge and the relative airflow vector. This angle is calculated as

$$\alpha_{\mathrm{e}} = \cos^{-1}\left(-\hat{\boldsymbol{b}}^{\mathrm{w}} \cdot \hat{\boldsymbol{v}}^{\mathrm{w}}\right), \quad \alpha_e \in [0, \pi). \tag{5}$$

where $\hat{\boldsymbol{b}}^{\mathrm{w}} = \begin{bmatrix} \cos\alpha & 0 & -\sin\alpha \end{bmatrix}^{\top}$ is the unit vector along the chord line in the direction from the trailing edge of the strip to its leading edge, and α is the feathering angle of the strip. We defined a second effective angle of attack α_{r} to set bounds on the values of the effective angle of attack so that it remains between 0 and $\pi/2$ radians. In the calculation of the lift and drag aerodynamic coefficients, the effective angle of attack was restricted between 0 and $\pi/2$ because the coefficients we used from (Han et al., 2015) were experimentally measured for the effective angles of attack only in this range.

$$\alpha_{\mathrm{r}} = \begin{cases} \alpha_{\mathrm{e}} & 0 \leq \alpha_{\mathrm{e}} \leq \frac{\pi}{2} \\ \pi - \alpha_{\mathrm{e}} & \frac{\pi}{2} < \alpha_e \leq \pi \end{cases} \tag{6}$$

Moreover, this definition of the effective angle of attack keeps the lift and drag coefficients positive and simplifies the model because the direction of the lift can just be specified by the lift force direction vector $\hat{\boldsymbol{f}}_{\mathrm{L}}$ elaborated in the next section.

Translational Aerodynamic Force. The translational aerodynamic force is the sum of the lift and drag forces on the wing and acts at the center of pressure. We assumed the center of pressure to be located on the wing at a distance one-quarter chord length behind the leading edge (green dashed line in Fig. 1G), because this is the region at which the bound vortex has been regarded to be concentrated according to the thin airfoil theory for both steady and unsteady aerodynamic effects (Ellington, 1984b). The lift and drag forces were calculated using the aerodynamic coefficients of hawkmoth *Manduca sexta* taken from (Han et al., 2015). The equations of these forces acting on a small wing strip of width dr are as follows (Cheng et al., 2016a).

$$d\boldsymbol{f}_{\mathrm{L}}^{\mathrm{w}} = \tfrac{1}{2}\rho C_{\mathrm{L}} v^2 c \; dr \; \hat{\boldsymbol{f}}_{\mathrm{L}}^{\mathrm{w}} \;, \tag{7}$$

$$d\boldsymbol{f}_{\mathrm{D}}^{\mathrm{w}} = \tfrac{1}{2}\rho C_{\mathrm{D}} v^2 c \; dr \; \hat{\boldsymbol{f}}_{\mathrm{D}}^{\mathrm{w}} \;, \tag{8}$$

where ρ is the air density, the aerodynamic coefficients (Han et al., 2015)

$$C_{\mathrm{L}}(\alpha_{\mathrm{r}}) = 1.552 \sin(\alpha_{\mathrm{r}}) \cos(\alpha_{\mathrm{r}}) + 1.725 \sin^2(\alpha_{\mathrm{r}}) \cos(\alpha_{\mathrm{r}}), \tag{9}$$

$$C_{\mathrm{D}}(\alpha_{\mathrm{r}}) = 0.0596 \sin(\alpha_{\mathrm{r}}) \cos(\alpha_{\mathrm{r}}) + 3.598 \sin^3(\alpha_{\mathrm{r}}), \tag{10}$$

v is the relative airflow speed of the strip, c and dr are chord length and width of a strip, and the translational drag and lift unit vectors, $\hat{\boldsymbol{f}}_{\mathrm{L}}$ and $\hat{\boldsymbol{f}}_{\mathrm{D}}$, are calculated as follows

$$\hat{\boldsymbol{f}}_{\mathrm{L}}^{\mathrm{w}} = \frac{\boldsymbol{q}^{\mathrm{w}}}{|\boldsymbol{q}^{\mathrm{w}}|}, \quad [11]$$

$$\hat{\boldsymbol{f}}_{\mathrm{D}}^{\mathrm{w}} = \hat{\boldsymbol{v}}^{\mathrm{w}}, \quad [12]$$

where

$$\boldsymbol{q}^{\mathrm{w}} = (\hat{\boldsymbol{v}}^{\mathrm{w}} \cdot \hat{\boldsymbol{n}}^{\mathrm{w}}) \left((\hat{\boldsymbol{v}}^{\mathrm{w}} \times \hat{\boldsymbol{n}}^{\mathrm{w}}) \times \hat{\boldsymbol{v}}^{\mathrm{w}} \right) \quad [13]$$

and $\hat{\boldsymbol{n}}^{\mathrm{w}}$ is the unit vector normal to the plane of the strip in its dorsal direction (see Fig. 1F). It is imperative to note that C_{L}, C_{D}, v, c, $\hat{\boldsymbol{f}}_{\mathrm{L}}$, $\hat{\boldsymbol{f}}_{\mathrm{D}}$ and α_{r} are functions of r. Their values vary for different blade element strips along the span of the wing. Moreover, our calculation of the unit vector $\hat{\boldsymbol{f}}_{\mathrm{L}}$ was sufficient to keep track of the direction of the lift force vector, without invoking a sign from the lift coefficient C_{L} outside the range of the effective angle of attack from 0 to $\pi/2$ radians. In the wing-attached coordinate frame, the total translational aerodynamic force on a strip is

$$d\boldsymbol{f}_{\mathrm{tra}}^{\mathrm{w}} = d\boldsymbol{f}_{\mathrm{L}}^{\mathrm{w}} + d\boldsymbol{f}_{\mathrm{D}}^{\mathrm{w}}. \quad [14]$$

Rotational Aerodynamic Force. In addition to the aerodynamic force due to translation of the wing, we also incorporated the aerodynamic force due to its rotation with angular velocity $\dot{\alpha}$ about the y^{w}-axis (Fung, 1969). This force was assumed to be acting perpendicular to a blade element strip at a distance half-chord behind the leading edge. This was based on the experimental results from (Han et al., 2015) on a dynamically scaled hawkmoth wing. In the wing-attached coordinate frame, the rotational aerodynamic force on a small wing strip of width dr is

$$d\boldsymbol{f}_{\mathrm{rot}}^{\mathrm{w}} = \rho C_{\mathrm{R}} v c^2 \dot{\alpha}\ dr \begin{bmatrix} -\sin\alpha \\ 0 \\ -\cos\alpha \end{bmatrix} \quad [15]$$

where the rotational aerodynamic coefficient $C_{\mathrm{R}} = \pi\left(0.75 - \frac{e}{c}\right)$, e is the distance between the leading edge and wing pitching axis, α is the wing pitching angle and $\dot{\alpha}$ is the the angular velocity of the wing pitching rotation (Cheng et al., 2016a; Ellington, 1984b).

Force due to Added-mass. While the wing is undergoing translational and rotational accelerations during flapping, it experiences an inertial force to accelerate the boundary layer of air around the wing surface. Assuming the moth is flying at a constant velocity (on average), most significant contributions to this force come from the wing accelerations $\ddot{\phi}$ and $\ddot{\alpha}$, and the velocity product $\dot{\phi}\dot{\alpha}$ due to the force being measured in a

non-inertial reference frame. This force acts perpendicular to a blade element strip at a distance half-chord behind the leading edge because the boundary layer is assumed to be uniformly distributed around a blade element strip (Truong et al., 2011). In the wing-attached coordinate frame, the force due to added-mass on a small wing strip of width dr is given by the following equation (Maybury and Lehmann, 2004).

$$d\boldsymbol{f}^{\mathrm{w}}_{\mathrm{adm}} = \frac{1}{4}\pi\rho\left(\left(\ddot{\phi}\sin\alpha + \dot{\phi}\dot{\alpha}\cos\alpha\right) rc(r)^2 + \frac{1}{4}\ddot{\alpha}c(r)^3\right) dr \begin{bmatrix} \sin\alpha \\ 0 \\ \cos\alpha \end{bmatrix}, \qquad [16]$$

where r is the distance of the wing strip from the wing hinge along the wing pitching axis.

Sum of Force Components. We numerically integrated each of the translational, rotational and added-mass aerodynamic force equations along the wing's spanwise length to evaluate the forces on the full right wing. Then we evaluated the sum of these forces and moments on the right wing in its wing-attached coordinate frame as follows

$$\boldsymbol{f}^{\mathrm{w}}_{\mathrm{right}} = \boldsymbol{f}^{\mathrm{w}}_{\mathrm{tra}} + \boldsymbol{f}^{\mathrm{w}}_{\mathrm{rot}} + \boldsymbol{f}^{\mathrm{w}}_{\mathrm{adm}}. \qquad [17]$$

Transformation to the Body-attached Frame. To explore how the aerodynamic forces act on the moth's body and affect its motion, we needed to transform the force vector calculated in the wing-attached frame to the body-attached frame. This was done in two steps. First, we transformed the instantaneous force vector from the wing-attached frame to the stroke-plane frame (through the wing kinematic angles ϕ and θ) as follows

$$\boldsymbol{f}^{\mathrm{sp}}_{\mathrm{right}} = \mathbf{R}_z(\phi)\mathbf{R}_x(\theta)\boldsymbol{f}^{\mathrm{w}}_{\mathrm{right}}\ , \qquad [18]$$

where

$$\mathbf{R}_x(\theta) = \begin{bmatrix} 1 & 0 & 0 \\ 0 & \cos\theta & -\sin\theta \\ 0 & \sin\theta & \cos\theta \end{bmatrix}, \quad \mathbf{R}_z(\phi) = \begin{bmatrix} \cos\phi & -\sin\phi & 0 \\ \sin\phi & \cos\phi & 0 \\ 0 & 0 & 1 \end{bmatrix} \qquad [19]$$

Second, we transformed from the stroke-plane frame to the body-attached frame (through the stroke-plane angle β, given that there is no body roll rotation) through another rotation matrix

$$\boldsymbol{f}^{\mathrm{b}}_{\mathrm{right}} = \mathbf{R}_y(-\beta)\boldsymbol{f}^{sp}_{\mathrm{right}} \qquad [20]$$

where

$$\mathbf{R}_y(-\beta) = \begin{bmatrix} \cos\beta & 0 & -\sin\beta \\ 0 & 1 & 0 \\ \sin\beta & 0 & \cos\beta \end{bmatrix}, \quad \boldsymbol{l}^{\mathrm{b}}_{\mathbf{1}} = l_1 \begin{bmatrix} \cos\chi_e \\ 0 \\ -\sin\chi_e \end{bmatrix}, \quad \chi_e = \chi + \chi_1.$$

The angle χ_e is the inclination angle of the wing hinge from the center of mass with respect to the horizontal plane, and is equal to the sum of body angle χ and the angle χ_1 as shown in Fig. 1H. The overall transformation from the wing-attached frame to the body-attached frame can also be represented as a single transformation matrix $\mathbf{R}_{\mathrm{w}}^{\mathrm{b}}$,

$$\boldsymbol{f}_{\mathrm{right}}^{\mathrm{b}} = \mathbf{R}_{\mathrm{w}}^{\mathrm{b}} \boldsymbol{f}_{\mathrm{right}}^{\mathrm{w}} \ , \qquad [21]$$

where $\mathbf{R}_{\mathrm{w}}^{\mathrm{b}} = \mathbf{R}_y(-\beta)\mathbf{R}_z(\phi)\mathbf{R}_x(\theta)$.

Induced power calculation. The induced power requirement for flight were also calculated for the two representative moth species. Induced power is the power required to impart sufficient momentum to the surrounding fluid in order to offset body weight as well as overcome the induced drag on the wing (Ellington, 1984c). The induced aerodynamic power calculation (Table A.1) was conducted following the method outlined in (Willmott and Ellington, 1997b). Additional details on induced power can be found in the Induced Power Calculation section.

RESULTS

Phylogeny. Phylogenetic relationships of the 57 bombycoid species used in this study (Fig. 2a; S1A) show similar relationships to those published previously (Breinholt et al., 2018; Hamilton et al., 2019; Barber et al., 2015; Kawahara and Barber, 2015; Rubin et al., 2018). We recovered a monophyletic clade (sister to Bombycidae) of the Sphinigidae and Saturniidae sister-families with a strong branch support values across the tree (Fig. S1A).

Hawkmoths and silkmoths each have diverse, but clustered forewing shapes in morphospace. The forewing shapes of hawkmoths and silkmoths are well separated in morphospace. Most of the variation (68%) in forewing shape is explained by the first two pPC axes (44% by pPC1 and 24% by pPC2; Fig. 2B;). pPC three and four explain 14% and 8% of the total variation, respectively (Fig. S2A;). All remaining pPCs each explained less than five percent of shape variation and a total of 10% of the variation. Projections into morphospace reveal that pPC1 generally corresponds to AR, where a low pPC1 value corresponds to a higher ratio between forewing length and width. High values of pPC2 corresponding to large rounded distal tips and low values of pPC2 corresponding to a narrower distal wing tip.

We found significant separation in morphospace using a MANOVA where scores of 4 pPCs were the response variables and clade (hawkmoth, silkmoth, ancient bombycoid lineages) was the factor (F = 14.912, $p = 2.33\times10^{-14}$). A second MANOVA that only included the hawkmoth and silkmoth clades (instead of all three groups) also reveals significant separation between these two clades (F = 44.42, $p = 6.612\times10^{-15}$), demonstrating that the differences are reflected in the split between hawkmoths and silkmoths. Additionally,

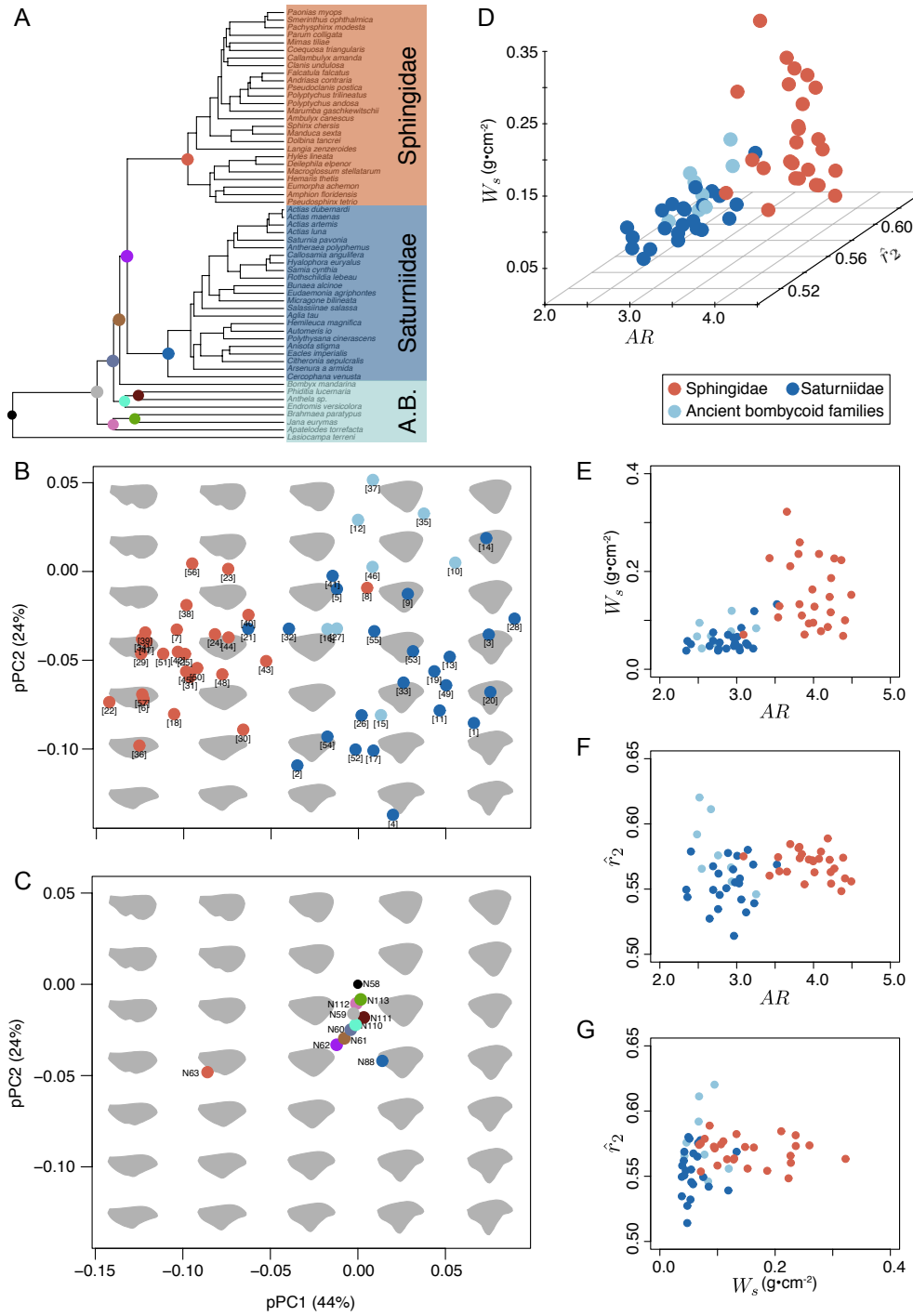

Fig. 2. The evolution and trajectory of forewing shape diversity. (A) The reconstruction of the phylogenetic relationships in bombycoids and outgroups (node labels in Fig. S1B). A.B. refers to Ancient Bombycoid lineages, which do not belong to either the Saturniidae or Sphingidae clades. Ancestral nodes are color coded for plotting in C. (B) Projections of the taxa onto the first two phylogenetic principal components demonstrates the separation of extant hawkmoths and silkmoths. The complete morphospace includes pPC 3 and 4 (Fig. S2A). The species-number key can be found in Fig. S2B (C) The ancestral state reconstruction of pPC1 and pPC2 scores reveals that forewing shape was conserved throughout the early evolutionary history of the Bombycoid superfamily until the ancestral hawkmoth (Node 63) and silkmoth (Node 88) rapidly diverged. (D) Species also cluster along aspect ratio (AR), wing loading (W_s), and radius of the second moment of area ($\hat{r}_2$). (E-G) Bivariate projections of panel D.

hawkmoths and silkmoths have significant separation along pPC1 (ANOVA, F = 131.94, $p = 3.035\times10^{-15}$), pPC3 (ANOVA, F = 27.48, $p = 3.688\times10^{-6}$), and pPC4 (ANOVA, F = 99.63, $p = 3.4\times10^{-13}$). Finally, both the hawkmoth and silkmoth clades have significantly distinct wing shapes from those of ancient bombycoids in 4D morphospace (MANOVA, Hawkmoths: F = 38.188, $p = 3.65\times10^{-11}$; Silkmoths: F = 3.3102, $p = 0.02555$).

We next tested if the hawkmoth and silkmoth clades have wing shape differences once accounting for phylogeny. Across the entire bombycoid phylogeny, wing shape along each pPC has significant phylogenetic signal (Table S2). This indicates that shape varies in some significant way across the phylogeny, but does not indicate where. Scores of pPC1, 3, and 4 have significant phylogenetic signal across a tree pruned to include both hawkmoths and silkmoths (Table S2). However, no phylogenetic signal was found when the tree is pruned to include only either the hawkmoths or the silkmoths (Table S2), indicating that forewing shape has significantly diverged at the node between the two sister families.

Distinct evolutionary trajectories of forewing diversification. We next reconstructed the ancestral trajectory of wing shape across the phylogeny, focusing on the differences that occur around the split between hawkmoths and silkmoths. Consistent with the phylogenetic signal test, the ancestral state reconstruction reveals that forewing shape was conserved (little variation in pPC score) until a distinct divergence at the nodes where hawkmoths and silkmoths split (Fig. 2C; Table S3). The range of pPC1 and pPC2 scores of the ancient nodes (nodes highlighted in 2 A, C) represent only 6.8% and 17.5% of the total variation in pPC scores of extant bombycoids (Fig. 2C) and are consistent with most of the shapes observed in the long branched "ancient bombycoid" families (Fig. 2B). The ancestral nodes of the hawkmoth (node 63) and silkmoth (node 88) sister families diverged from this cluster, indicated by minimal overlap in the 95% confidence interval of the state of these two nodes (Table S3). From these two sister nodes, each group speciated and underwent subsequent diversification. However, while individual hawkmoth or silkmoth species might have somewhat more convergent or divergent wing shapes, the two groups maintain distinct differences, especially in pPC1.

Aerodynamic features of the wing and body also separate between clades. The pPCA is a data-driven analysis of overall differences in shape. In order to relate variation in forewing shape to metrics classically used in aerodynamics, we also quantified several specific forewing and body shape variables: wing length (R), wing mean chord length ($\bar{c}$), wing area (S), the nondimensional radius of second moment of wing area ($\hat{r}_2$), wing aspect ratio (AR), wing loading (W_s), body length (l_b), abdomen length (l_{abd}), the fraction of body length occupied by the abdomen ($\hat{l}_{\text{abd}}$) and thorax ($\hat{l}_{\text{tho}}$), respectively, and an estimate of total body mass (m_t) (Summary data: Table 1). Before accounting for phylogeny, significant differences were

found between hawkmoths and silkmoths for each trait other than m_t (Table 1). Notably, R, $\bar{c}$, and S are significantly greater in silkmoths than in hawkmoths, while AR, W_s, and $\hat{r}_2$ are all significantly greater in hawkmoths than in silkmoths. While variation in l_b spans similar ranges within each family, clade average l_b and $\hat{l}_{\text{abd}}$ are significantly longer in hawkmoths than silkmoths (Table 1), and $\hat{l}_{\text{tho}}$ is generally greater in silkmoths than in hawkmoths, (Table 1).

In order to determine if these morphological variables also diverged between hawkmoths and silkmoths, we again measured phylogenetic signal for each trait. As with the pPCs, significant phylogenetic signal is present when silkmoths and hawkmoths are combined, but not when the tree is pruned to consider each family individually (Table 1; S2). The only exception is W_s, which shows significant phylogenetic signal within only the hawkmoths. The lack of phylogenetic signal within the families means that the primary pattern of divergence occurs at the split of the two clades. However, given the limitations of phylogenetic sampling, specific individual hawkmoth or silkmoth taxa might still significantly diverge from the rest of the larger families.

We also reconstructed the ancestral states of the three most commonly used wing shape metrics: AR, W_s, and $\hat{r}_2$ (Fig. 3A-C). Each trait was conserved with large confidence intervals at the rootward nodes (Fig. 3; Table S3). However, at the nodes representing the ancestors of the hawkmoth and silkmoth clades, significant patterns of divergence are found for AR (no overlap in confidence intervals; Table S3) and W_s (minimal overlap in confidence intervals; Table S3). Taken together both the data driven pPC morphospace and the specific measures of forewing shape most related to aerodynamics are first conserved and diverge precisely at the split of hawkmoths and silkmoths.

Wing beat frequency, but not inertial power, diverges between hawkmoths and silkmoths. Wing beat frequency and the power required to accelerate the mass of the wings each wingstroke (inertial power – P_{acc}) are both important values that depend on wing size. Lacking wing kinematics for all the museum specimens, n was estimated from scaling relationships (Table A.1; (Deakin, 2010)). In our analysis, n is distinct from wing shape, but not independent of wing size variation. The P_{acc} calculation relies on variables of m_t and m_w, which were estimated from museum specimens by assuming the body has a density equal to water (Ellington, 1984a). Mean n is significantly greater in hawkmoths (mean ± SD: 33.92 ± 11.23 Hz) compared to silkmoths (mean ± SD: 17.47 ± 5.56 Hz; $p<0.0001$), but there is no significant difference in P_{acc} between the hawkmoth and silkmoth clades (hawkmoths: 48.65 ± 12.97 w kg^{-1}, silkmoths: 41.57 ± 8.50 w kg^{-1}; $p>0.05$; Table 1). n diverges between hawkmoths and silkmoths early in the evolutionary history of bombycoids (Fig. 3E). n at the ancestral nodes for the hawkmoth and silkmoth clades are estimated to be 34.28 Hz (95% confidence interval: 27.10 – 41.47) and 22.88 Hz (95% confidence interval: 14.35 – 31.41), respectively. Prior to that split, the ancestral state of P_{acc} is equivocal at rootward nodes

	Average ± stdev			T-test		
	Ancient bombycoids	Silkmoths	Hawkmoths	*p* (AB-S)	*p* (AB-H)	*p* (S-H)
R (m)	0.0349 ± 0.017151	0.0516 ± 0.01638	0.04197 ± 0.0150	0.02012	0.26813	0.03706
$\bar{c}$ (m)	0.0128 ± 0.006359	0.0179 ± 0.0056	0.01058 ± 0.0036	0.04038	0.22018	<0.0001
S (m^2)	0.0005 ± 0.000524	0.0010 ± 0.00058	0.00049 ± 0.00033	0.05346	0.77188	0.00034
$\hat{r}_2$	0.5792 ± 0.026389	0.5539 ± 0.01769	0.56927 ± 0.01034	0.00478	0.12092	0.00046
AR	2.7600 ± 0.265587	2.88959 ± 0.28949	3.96152 ± 0.337358	0.27537	<0.0001	<0.0001
l_b (m)	0.0272 ± 0.010591	0.02852 ± 0.007602	0.03699 ± 0.010579	0.69850	0.02837	0.00260
m_t (g)	0.7855 ± 0.78914	1.19349 ± 0.83900	1.59744 ± 1.419522	0.23925	0.13448	0.23920
n (Hz)	26.5094 ± 9.630467	17.4708 ± 5.56408	33.9163 ± 11.22714	0.00291	0.10248	<0.0001
W_s (g•cm^{-2})	0.0749 ± 0.025196	0.05971 ± 0.024333	0.15295 ± 0.069721	0.14164	0.00427	<0.0001
$\hat{l}_{tho}$	0.3008 ± 0.059889	0.32948 ± 0.032573	0.29120 ± 0.029230	0.09752	0.53970	<0.0001
$\hat{l}_{abd}$	0.6351 ± 0.06688	0.61704 ± 0.04127	0.64521 ± 0.035400	0.37452	0.57503	0.01334
l_{abd} (m)	0.0175 ± 0.007939	0.01771 ± 0.00534	0.023979 ± 0.007354	0.94196	0.04087	0.00150
pPC1	0.0114 ± 0.0244	0.0222 ± 0.0412	-0.0961 ± 0.0306	0.493	<0.0001	<0.0001
pPC2	-0.0031 ± 0.043370	-0.0563 ± 0.03847	-0.0465 ± 0.025442	0.002	0.001	0.2910
pPC3	-0.0004 ± 0.014623	0.0016 ± 0.02405	-0.0366 ± 0.026721	0.815	0.001	<0.0001
pPC4	-0.0050 ± 0.016029	-0.0181 ± 0.02798	0.0452 ± 0.015287	0.224	<0.0001	<0.0001
P_{acc}	33.0317 ± 11.13033	41.5706 ± 8.49548	48.6594 ± 12.97370	0.03143	0.00434	0.0306

Table 1. Clade averaged wing and body measurements with corresponding statistics. Adjusted alpha = 0.0027778

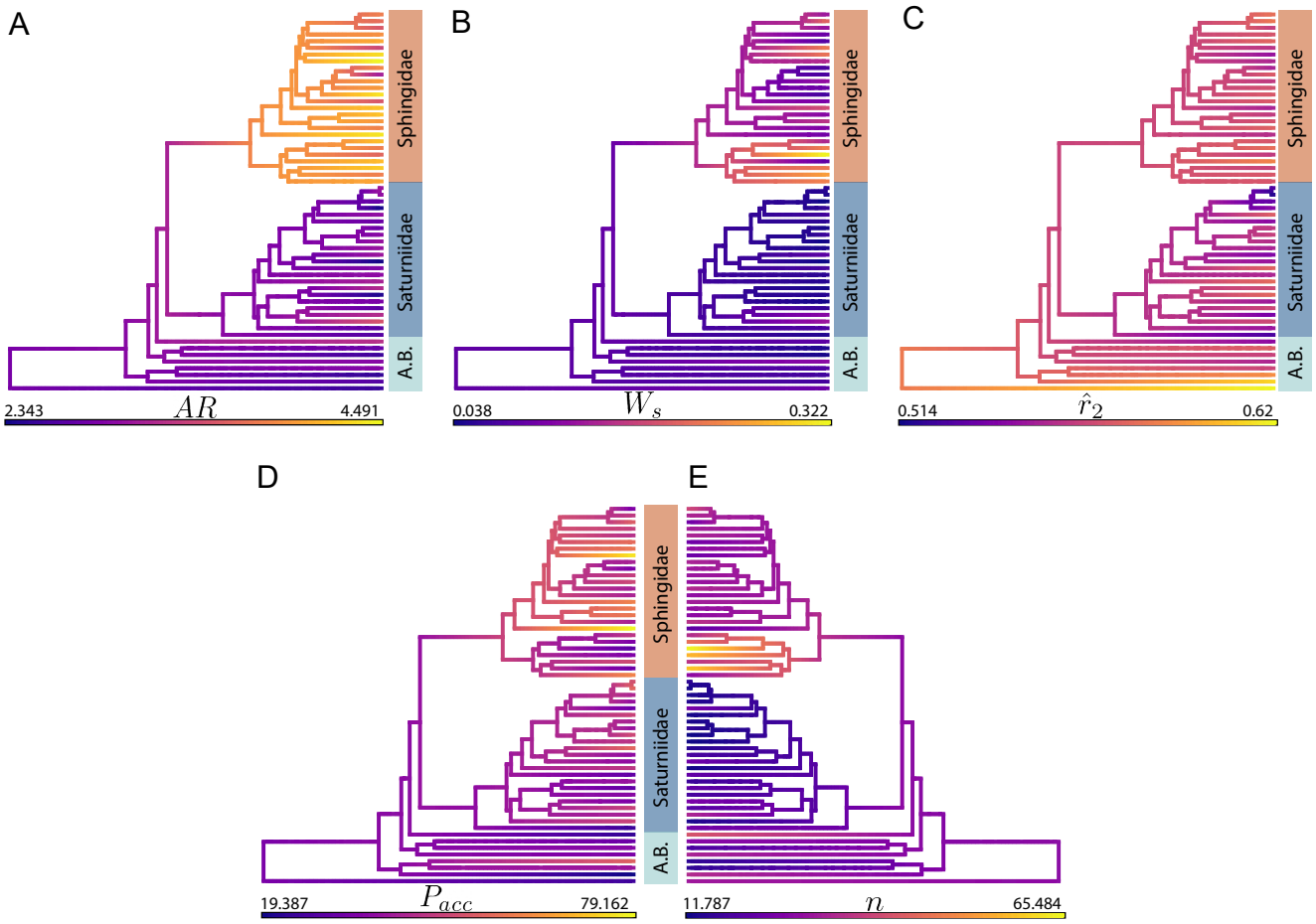

Fig. 3. Maximum likelihood ancestral state reconstructions of morphological variables. Ancestral state reconstructions of (A) aspect ratio (AR) and (B) wing loading (W_s) diverge between the hawkmoth and silkmoth sister clades. The reconstruction of (C) radius of second moment of wing area ($\hat{r}_2$) is more conserved across bombycoids, but is generally shifted towards higher values in hawkmoths than silkmoths. Finally, (D) inertial power (P_{acc}) is conserved across the superfamily with no divergence between hawkmoths and silkmoths. The reconstruction of (D) wing beat frequency (n) also reveals strong divergence between the hawkmoth and silkmoth clades. The hawkmoth subfamily, Macroglossinae (Node 82), is a notable example of particularly high n.

(Fig. 3D; Table S3), and remains generally conserved over time. Finally, significant phylogenetic signal is found in n over the tree pruned to include only silkmoths and hawkmoths, and is also found when the tree is pruned to only include either silkmoths or hawkmoths (Table 1, S2). However, no phylogenetic signal is found for P_{acc} (Table S2).

Three-dimensional body and forewing kinematics are different between the exemplar hawkmoth and silkmoth. To determine the impact of wing movement on aerodynamic force production, we chose a species of hawkmoth (*E. achemon taxa #29* in Fig. 2B) and silkmoth (*A. luna – taxa #3* in Fig. 2B) that represent the more divergent regions of morphospace (Fig. 4A, B; Fig. 2B). Three individuals from each species were recorded conducting steady forward flight (Fig. 4C, D). *A. luna* had a lower n, more steeply inclined stroke plane, β, and larger wingstroke sweep, ϕ, and deviation, θ, amplitudes (Table 2; Fig. 4C, D). In comparison, *E. achemon* utilizes a greater $\overline{\phi}$ and α amplitude throughout a wing stroke (Fig. 4C, D).

Wingstroke averaged forces are comparable between species. Given that the *A. luna* and *E. achemon* use their wings in different ways in addition to having different wing shapes, we next assessed the overall aerodynamic force and power implications between the two species. Despite an interspecific difference in wing area of a factor of 3.12, the peak and wingstroke averaged body centered forces are similar in magnitude between species (Table 3). The within wingstroke force profiles do show different patterns, especially in f_x^b during the first half of wing stroke and f_z^b during the second half of wing stroke; in both cases, these forces are predominately positive in *A. luna* and negative in *E. achemon* (Fig. 5a). Although the magnitude of rotational (f_{rot}^b) and added mass (f_{adm}^b) forces are generally larger in *A. luna* in comparison to *E. achemon* (Fig. 6A), these forces tend to act in opposition, and interspecific differences in the total body forces (f_{tot}^b) are primarily due to translational force, f_{trans}^b (Fig. 6A). To assess if flight speed might contribute to difference in aerodynamics, we conducted an additional model where the horizontal and vertical velocities are set to the species average recorded during free flight. Doing so resulted in the same patterns of force (Fig. S3A-B).

Actias luna and Eumorpha achemon have similar induced aerodynamic power requirements. While *E. achemon* and *A. luna* have nearly the same magnitude wing stroke averaged f_{tot}^b, the n of *E. achemon* is approximately double that of *A. luna* ($E.a = 31.50$; $A.l = 14.20$). Therefore, when comparing wing-stroke averaged force production per unit time, *E. achemon* produces approximately twice the force in a given amount of time in comparison to *A. luna*. These interspecific differences in force production per unit time are paralleled by an interspecific difference in the induced power (P_{ind}) requirement. The P_{ind} requirement of *E. achemon* is 13.758 W kg^{-1}, while the P_{ind} requirement of *A. luna* is 5.52 W kg^{-1} (Table 3).

Measured wing kinematics								
	Eumorpha achemon				*Actias luna*			
	***E.a.* 1**	***E.a.* 2**	***E.a.* 3**	**Mean ± stdev.**	***A.l.* 1**	***A.l.* 2**	***A.l.* 3**	**Mean ± stdev.**
n (Hz)	31.75	33.33	29.41	31.50 ± 1.97	15.38	13.33	13.89	14.20 ± 1.06
β (deg.)	42.04	22.94	36.93	33.97 ± 9.89	88.81	74.70	64.14	75.88 ± 12.37
χ_{p-p} (deg.)	3.95	9.91	4.05	5.97 ± 3.41	30.02	25.80	22.32	26.05 ± 3.86
$\overline{\chi}$ (deg.)	26.83	36.35	34.48	32.55 ± 5.04	12.57	27.76	23.14	23.14 ± 9.18
ϕ_{p-p} (deg.)	115.34	96.39	120.64	109.51 ± 12.74	129.01	132.55	135.78	127.80 ± 3.38
$\bar{\phi}$ (deg.)	24.03	31.82	6.28	19.87 ± 13.14	9.22	10.76	15.67	11.03 ± 3.42
ϕ_{min} (deg.)	-30.95	-15.55	-49.32	-31.70 ± 16.91	-52.72	-51.60	-50.86	-51.44 ± 0.94
ϕ_{max} (deg.)	84.38	80.84	71.31	77.81 ± 6.76	76.29	80.95	84.92	76.36 ± 4.32
θ_{p-p} (deg.)	6.23	9.04	22.24	11.41 ± 8.55	17.41	22.84	22.81	19.64 ± 3.12
$\bar{\theta}$ (deg.)	-2.71	-0.95	1.90	-0.56 ± 2.36	2.98	-3.20	3.81	1.18 ± 3.89
θ_{min} (deg.)	-4.92	-5.05	-6.47	-4.71 ± 0.86	-6.63	-18.86	-8.03	-10.52 ± 6.69
θ_{max} (deg.)	1.27	3.99	15.77	6.70 ± 6.29	10.78	3.89	14.78	9.13 ± 5.46
α_{p-p} (deg.)	70.61	92.09	90.11	80.91 ± 11.87	53.00	49.98	54.87	45.08 ± 2.47
$\bar{\alpha}$ (deg.)	77.08	87.67	88.74	84.56 ± 6.43	88.37	76.85	81.44	82.14 ± 5.82
α_{min} (deg.)	44.12	54.43	47.04	50.14 ± 5.31	60.43	51.77	56.53	58.49 ± 4.34
α_{max} (deg.)	115.46	146.41	136.78	133.02 ± 15.84	112.76	102.18	108.66	101.54 ± 5.33

Fourier coefficients fit to species mean wing kinematics					
		E. achemon		*A. luna*	
Kinematic variables	***k***	***a***	***b***	***a***	***b***
$\phi(t)$	0	0.4006	0	0.2165	0
	1	0.9480	-0.0711	1.0910	-0.0309
	2	0.0074	-0.0839	0	0
	3	0	0	0	0
$\theta(t)$	0	-0.0133	0	0.022	0
	1	-0.0168	-0.0742	-0.0025	-0.1448
	2	-0.0403	-0.0064	0.0337	0.0102
	3	-0.0082	0.0152	-0.0037	0.0261
$\alpha(t)$	0	1.4723	0	1.4360	0
	1	-0.0525	-0.6877	0.0022	-0.3856
	2	-1.597	-0.0620	0.0419	0.0101
	3	0	0	0.0059	-0.0123

Table 2. Summary of comparative wing kinematics for the representative hawkmoth and silkmoth species.

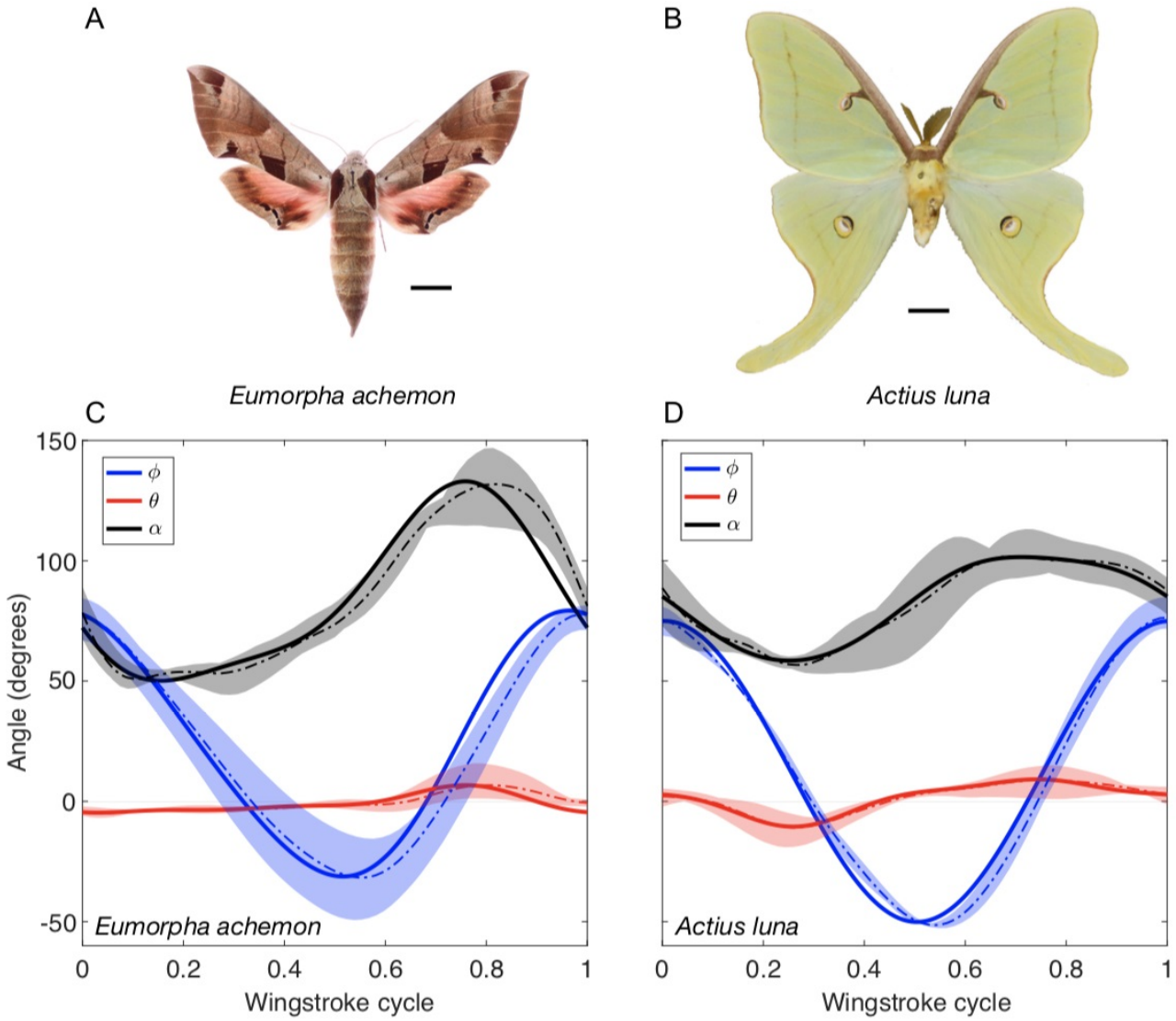

Fig. 4. Three-dimensional wing kinematics of a representative hawkmoth and silkmoth. *E. achemon* (A) *A. luna* (B) were flown in a wind tunnel to obtain three-dimensional kinematics (C and D). Scale bars are equal to 1 centimeter. For both species, we measured sweep (ϕ, blue), deviation (θ, red), and morphological feathering (α, black) angles. The shaded region of each curve represents the range of values recorded, the dashed lines represent the species mean, and the solid line represents the third order Fourier fit, used in all aerodynamic models. N = 3 individuals per species and one wing stroke per individual. The mean n is 14.2 in *A. luna* and 31.5 in *E. achemon* (Table 2).

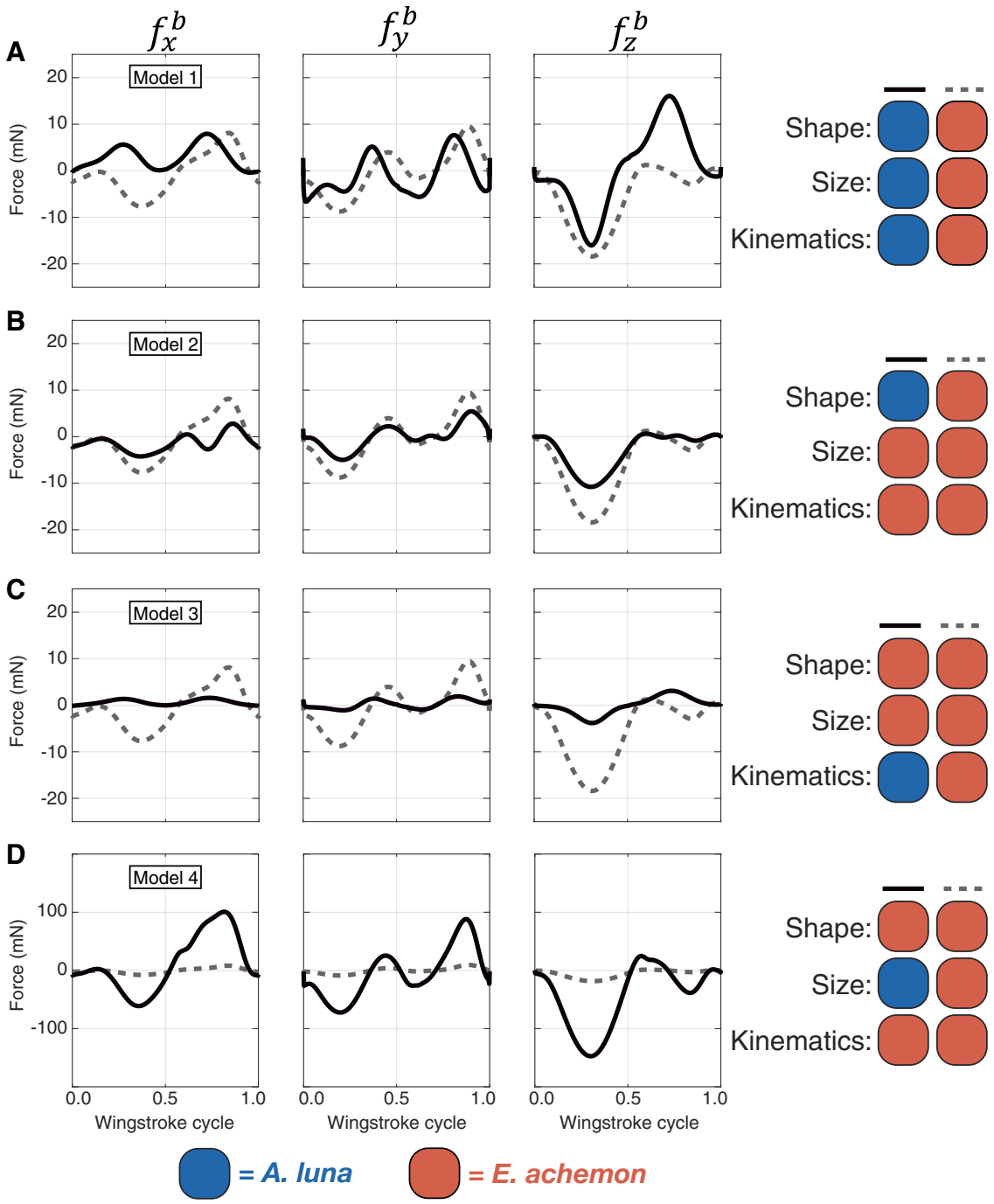

Fig. 5. Quasi-steady aerodynamic force production by the right wing in the body-centered coordinate system. Column one, two, and three display the f_x^b, f_y^b, and f_z^b, respectively. The two wings of each model are identified by solid and dashed lines, respectively. The dashed line is the same in each model. The key on the right side of each model can be used to determine the specific wing shape and movement parameters used for each wing. Red represents variables from *A. luna* and blue represents variables from *E. achemon*. (A) Model 1 compares interspecific aerodynamics between *A. luna* (solid line) and *E. achemon* (dashed line). Models 2 (B), 3 (C), and 4 (D) investigate how aerodynamics are impacted by changes in wing shape, movement, and size, respectively. All forces are only presented for a single right wing. The negative f_z^b direction points upward and the positive f_x^b direction points forward in the coordinate system.

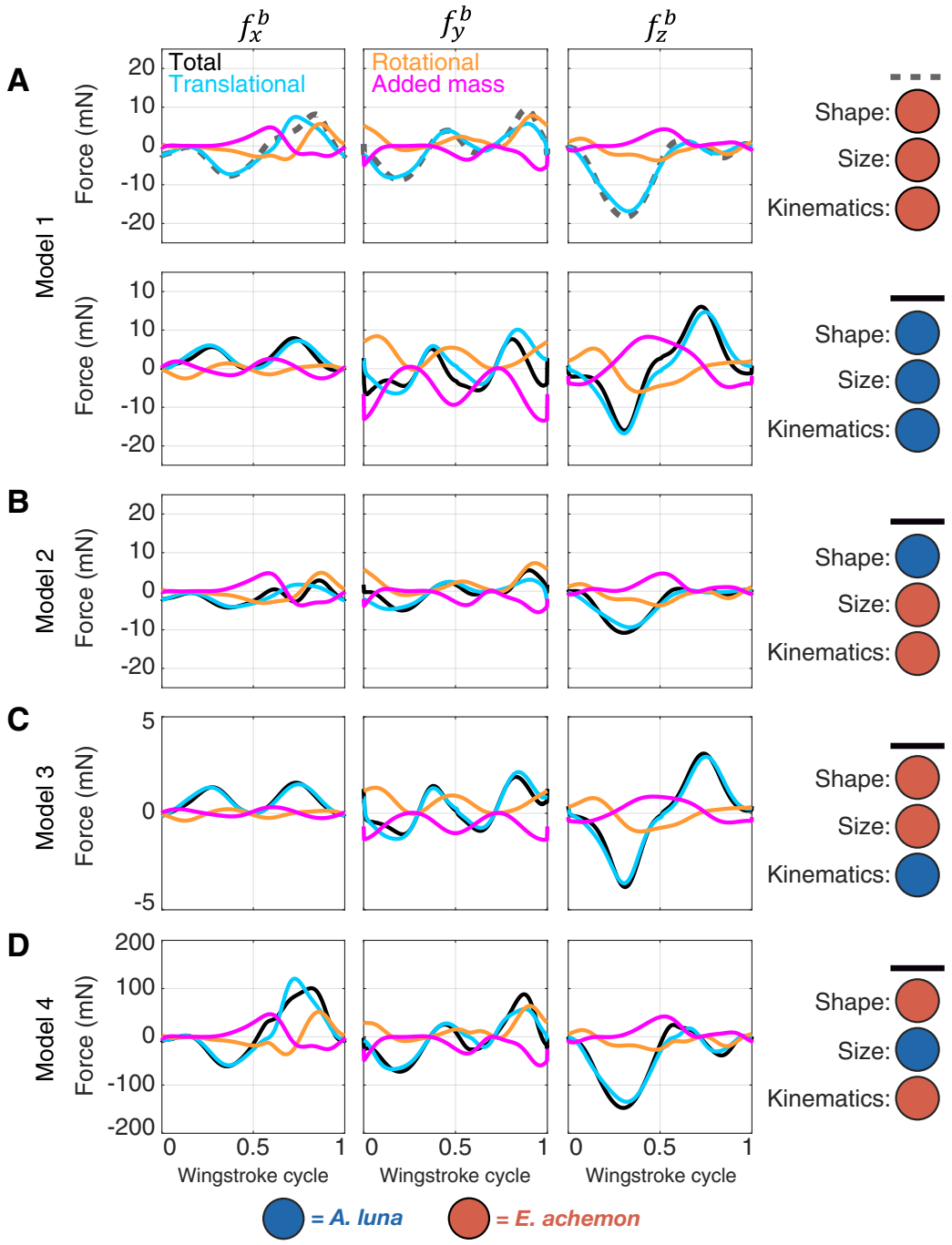

Fig. 6. Translational, rotational, and added mass components of aerodynamics force. Details of the four models are identical to those in Figure 5. Color schemes for component are the same for both species. Black represents the total force, cyan represents the translational force component (f^b_{trans}), gold represents the rotational force component (f^b_{rot}), and pink represents the added mass force component (f^b_{adm}). Column one, two, and three display the f^b_x, f^b_y, and f^b_z, respectively. All forces are only presented for a single right wing. In all four models for each species, f^b_{trans} drives the majority of the pattern in total force throughout the wing stroke.

		$\bar{f}^b_{tot}$ (N)			$\bar{f}^b_{trans}$ (N)			$\bar{f}^b_{rot}$ (N)			$\bar{f}^b_{adm}$ (N)			Induced Power (W/kg)
Model	Species	x	y	z	x	y	z	x	y	z	x	y	z	
1	*E. a.*	-0.545	-0.282	-5.714	-0.692	-0.606	-5.513	-0.243	1.974	-1.162	0.39	-1.65	0.96	13.758
	A. l.	2.915	-1.023	0.402	3.097	0.771	-0.47	-0.244	3.421	-0.422	0.062	-5.216	1.294	5.52
2	*E. a.*	-0.545	-0.282	-5.714	-0.692	-0.606	-5.513	-0.243	1.974	-1.162	0.39	-1.65	0.96	13.758
	A. l.	-1.342	-0.022	-3.022	-1.192	-0.394	-3.099	-0.269	1.891	-1.088	0.119	-1.519	1.165	7.747
3	*E. a.*	-0.545	-0.282	-5.714	-0.692	-0.606	-5.513	-0.243	1.974	-1.162	0.39	-1.65	0.96	13.758
	A. l.	0.648	0.193	-0.093	0.66	0.212	-0.15	-0.039	0.546	-0.075	0.027	-0.564	0.132	8.962
4	*E. a.*	-0.545	-0.282	-5.714	-0.692	-0.606	-5.513	-0.243	1.974	-1.162	0.39	-1.65	0.96	13.758
	A. l.	12.085	-4.914	-43.778	9.627	-3.588	-44.082	-1.351	14.777	-9.07	3.809	-16.103	9.374	11.629

Table 3. Wing stroke averaged total and component forces produced by each species across models.

Aerodynamic force production is impacted by interspecific differences in wing size, shape, and movement. To assess how size, shape and kinematics impact the aerodynamics, we created several intermediate models that separate their contributions. The base comparison reported above (Model 1 – Figs. 5A, 6A) uses each species' own wing shape, size, kinematics (ϕ, θ, and α), n, and β, with forward flight velocities set to 2 m/s. In Model 2 (Figs. 5B, 6B) we set wing kinematics and size to be that of *E. achemon* in both cases, leaving interspecific differences only in wing shape. In Model 3 (Figs. 5C, 6C), we set wing shape and size to be that of *E. achemon*, leaving interspecific differences only in wing kinematics. Finally, in Model 4 (Figs. 5D, 6D), we set wing shape and kinematics to be that of *E. achemon*, leaving interspecific differences only in wing size.

Wing shape:. The *E. achemon* wing shape produces larger net aerodynamic forces than *A. luna* shaped wings (Figs. 5B; 6B). The primary determinant of this increase in f^b_{tot} is the greater f^b_{trans} (Fig. 6B). While different in average and peak magnitude, the pattern of the f^b_{trans} (as well as the rotational and added mass forces) throughout the wing stroke was generally similar in both wing shape cases (Fig 6B; Table 3). The small interspecific differences that exist in the shape of f^b_x and f^b_z during the second half of wing stroke (Fig. 5B) occur because the magnitude of the translational force component of *A. luna* shaped wings is decreased relative to the magnitude of the added mass and rotational force components (Fig. 6B). The increase in the relative contribution of f^b_{rot} and f^b_{adm} in *A. luna* is responsible for the interspecific differences in the shape of $f^b_x$and f^b_z during the second half of wing stroke (Figs. 5B, 6B).

Wing kinematics:. The most apparent interspecific difference in aerodynamics due to kinematics alone (Model 3) is that *A. luna* produces much lower overall forces than *E. achemon* (Fig. 5C). The reduction in total body forces is again determined primarily by differences in translational force (Fig. 6C). The main cause of this difference is that n, and hence wing velocity, of *E. achemon* is 2.2 times greater than *A. luna* (Table 2. Interspecific differences in kinematics are also responsible for interspecific differences in the sign of f^b_x and f^b_z in Model 1 during the first half and second half of wing stroke, respectively (Fig. 5A). To break this

down further, we separated the contributions of stroke plane angle (β), wing angles (ϕ, θ, and α) and n (Fig. S3). The interspecific sign flip in f_z^b (Fig. 5A) occurs due to a combination of stroke plane angle and angle of attack (Fig. S3A), and the f_x^b sign flip (Fig. 5A) occurs primarily from the more vertical stroke plane (larger β) of *A. luna* (Fig. S3C).

Wing size:. *A. luna* has larger wings and, if all other variables are equal (Model 4), it is not surprising that *A. luna* produces larger overall forces (Figs. 5D, 6D). As before, differences in total force are primarily due to differences in the translational force (Fig. 6D). However, the magnitude of the rotational and added mass components of f_x^b, f_y^b, and f_z^b are also nearly an order of magnitude larger in *A. luna* sized wings compared to *E. achemon* (Fig. 6D). Overall, wing size has the predictable effect of scaling all of the force components. Taken together, the three knobs (shape, kinematics, and size) that evolution can tinker with means that even though the wing shapes are quite distinct between hawkmoths and silkmoths, these differences converge on similar overall wingstroke averaged forces (but different within wing stroke patterns) from different combinations of morphology and kinematics.

DISCUSSION

Wing shape can have a strong influence on the aerodynamics and maneuverability of flying animals. The first goal of this study was to test if hawkmoths and silkmoths diverged signifcantly in wing shape across the moth superfamily Bombycoidea. We find that early in the evolutionary history of Bombycoidea, wing shape was generally conserved until the ancestors of the hawkmoth and silkmoth sister clades rapidly separated in morphospace (Fig. 2C). The evolutionary split between these two families has been dated to occur between 57 and 75 MYA (Kawahara et al., 2019), suggesting that these wing shape trajectories have been evolving since then.

The distinct trajectory in wing shape change between hawkmoths and silkmoths was followed by a subsequent shape diversification within each group. Even specific species within each group that subsequently converged in life history did not fully converge to employ overlapping wing shapes. For example, while the majority of adult hawkmoths are known for their hovering nectaring behavior, members of the hawkmoth subfamily, Smerinthinae (Node 67; Figs. S1B, 2A), have lost the ability to feed as adults (Tuskes et al., 1996), convergent with all species of silkmoth. However, the wing shape of Smerinthinae species remains divergent with silkmoths with the exception of *Andriasa contraria* (Taxon 8). While we chose species to broadly cover the groups within bombycoids, sampling is far from complete. Therefore, we remain conservative in our interpretation, focusing on the split between hawkmoths and silkmoths for which we were able to accumulate broad sampling for our analysis. In sum, these data provide phylogenetic evidence supporting our hypothesis that there have been distinct wing shape trajectories in these two groups of

bombycoids.

Sillkmoth wing shapes are more favorable to maneuverability than hawkmoths. The evolution of forewing shape does not support hypotheses based on the presumed maneuverability of hawkmoths. We find that hawkmoths employ wings of high AR, W_s, and $\hat{r}_2$; all metrics typically associated with low degrees of maneuverability. In contrast, we find that silkmoths are employing wings of low AR, W_s, and $\hat{r}_2$; all metrics typically associated with higher degrees of maneuverability. However, these relationships between wing shape and maneuverability are typically used in fixed wing aircraft theory or when the kinematics of the flapping wing are held constant. In species employing flapping flight, wing shape and movement could undergo correlated evolution to produce species-specific performance metrics that could not be predicted by either wing shape or movement alone.

The high aspect ratio wings of hawkmoths and larger wing stroke amplitude of silkmoths lead to similar induced power requirements. In comparison to silkmoths, hawkmoths evolved high AR wings (Figs. 2, 3; Table 1) which might reduce maneuverability; however, high AR also reduce the induced power (P_{ind}) requirements of flight (Norberg and Rayner, 1987; Pennycuick, 1968). P_{ind} is the power required to overcome induced drag on the wing and impart sufficient downwards momentum to the surrounding air to offset body weight. The reduced maneuverability of high AR wings is due to an increase in the moments of inertia of the wing pair (Betts and Wootton, 1988), but the hawkmoth AR increase is concomitant with a reduction in wing area. Hawkmoths have evolved high AR by reducing mean chord length, $\bar{c}$, rather than through an increase in wing span, R (Table 1; Fig 2B). Therefore, while selection for economical flight (increased AR) might often reduce maneuverability, the evolution of short, high AR wings in hawkmoths (achieved through a reduction in $\bar{c}$) could act to increase economy while not necessarily sacrificing maneuverability. The potential cost is that proportionally smaller wings could reduce wing stroke-averaged aerodynamic force production, if wing movement remains constant. However, our aerodynamic model (Figs. 5A; 6A) reveals that the changes in wing kinematics, and particularly the higher wingbeat frequencies of hawkmoths, result in very similar wing stroke averaged forces between *E. achemon* and *A. luna*.

Despite employing lower AR wings, the representative silkmoth, *A. luna*, does not have a greater induced power (P_{ind}) requirement than the representative hawkmoth, *E. achemon*. The higher AR wings of hawkmoths leads to the prediction that hawkmoths would require less P_{ind} than silkmoths (Pennycuick, 1968). However, P_{ind} required for flight is also inversely proportional to both R and wing stroke amplitude ($\phi_{\text{p-p}}$). The kinematics from our two representative species show that the silkmoth (*A. luna)* employs a greater $\phi_{\text{p-p}}$ in comparison to the hawkmoth (*E. achemon*) (Fig. 4; Table 2). The net effect of AR, R, and $\phi_{\text{p-p}}$ is that there is little difference in the P_{ind} requirement between these two species, with *A. luna*

actually being somewhat lower.

The employment of smaller, high AR wings by hawkmoths and the production of a large amplitude wingstrokes by silkmoths are two different strategies that can act to reduce the P_{ind} requirements of flight. Many hawkmoth species are known for their ability to sustain long duration bouts of hovering, often associated with nectaring from flowers (Sprayberry and Daniel, 2007; Wasserthal, 1993, 1998), which require a high-power output. In contrast, all silkmoths employ rudimentary mouth parts and do not feed as adults (Janzen, 1984; Tuskes et al., 1996). Therefore, in hawkmoths, the selective pressure to reduce power while not sacrificing maneuverability has likely driven the evolution of short, high AR wings used at a high n. In silkmoths, the selective pressure to increase lifespan (endurance) has likely driven the evolution of large wing beat amplitudes used at a low n. Kinematic differences (particularly n and $\phi_{\text{p-p}}$) parallel the broader clade specific wing shape differences in AR. Hawkmoths and silkmoths have therefore evolved different strategies to reduce P_{ind}.

While P_{ind} is one of three components of the total aerodynamic power requirement, at slower flight speeds, which were employed by our exemplar species, the majority of the total aerodynamic cost in *Manduca sexta*, a species of hawkmoth, is from P_{ind} (Willmott and Ellington, 1997b). Inertial power requirements are similar between our exemplar species and the similar body size between the exemplar species suggests similar parasitic power requirements. The difference in wing area between our exemplar species does suggest, however, that *A. luna* will incur greater profile power costs in comparison to *E. achemon*. However, we suggest that the reduced P_{ind} of *A. luna* in comparison *E. achemon* ultimately leads to similar overall aerodynamic power requirements between the two species.

Hig wing beat frequency might act to offset high wing loading (W_s) in hawkmoths. The lower W_s of silkmoths suggests they are more maneuverable than hawkmoths, but, as before, this assumes all other things are equal. The reduced W_s of silkmoths comes primarily from a larger S rather than smaller body size compared to hawkmoths (Table 1). Higher W_s reduces mass-specific wing-stroke averaged forces. However, many species use increased flight speeds or high n to offset a high W_s in terms of aerodynamic force production (Ahmad, 1984; Byrne et al., 1988). Therefore, one selective pressure that could have led to the evolution of a higher n in hawkmoths is the need to offset the greater magnitude of W_s relative to silkmoths and other bombycoid families.

The greater radius of second moment of area ($\widehat{r_2}$) of hawkmoths can augment force production. The high $\widehat{r_2}$ of hawkmoth wings again suggests that silkmoths should be more maneuverable than hawkmoths (Le Roy et al., 2019; Ellington, 1984a). For a wing of uniform thickness and density, larger $\widehat{r_2}$ means more mass is concentrated distally along the wingspan, corresponding to an increase in moments of inertia. In

fixed wing aircrafts, larger wing moments of inertia hinder yaw and roll maneuvers (Etkin and Reid, 1996). However, in flapping or revolving wings, when all other things are equal, the larger $\widehat{r_2}$ of hawkmoths would also increase their magnitude of torque production relative to silkmoths. The velocity of a wing section increases with its distance from the axis of rotation, and aerodynamic force production is proportional to velocity squared. Shifting more area distally (increasing $\widehat{r_2}$) means more of the wing is moving at higher speeds enhancing production of aerodynamic forces and torques (e.g. Muijres et al. (2017); Fernandez et al. (2017)).

We can see this pattern when comparing aerodynamic force production between our representative hawkmoth (*E. achemon*) and silkmoth (*A. luna*) species. In Model 2, where wing area and all kinematic parameters are equal between species, the f_x^b, f_y^b, and f_z^b traces follow similar trajectories across the wing stroke and the magnitude of every force is greater in *E. achemon* shaped wings than in *A. luna* shaped wings (Fig. 5B; 6B).

Large, slow wings might produce bobbing flight in silkmoths. We find that the complex interaction between wing shape, size, and kinematics are tightly linked to produce the within wingstroke aerodynamic forces of *A. luna* and *E. achemon* (Figs. 5A, 6A), and might contribute to the differences in flight behavior between the families. *A. luna* has more variation in forces during the wingstroke even though it produces approximately the same average force as *E. achemon*. This is especially noticable in the switch from negative f_z^b to positive during the wingstroke in *A. luna*. Large force fluctuations and asymmetry (Figs. 5A, 6A) should lead to greater fluctuation in body vertical velocity and are likely the source of the bobbing, erratic motions that are characteristic of silkmoths and may be useful in predator avoidance.

Evolution of high wing beat frequency (n) enables hawkmoth maneuverability with wing shape to reduce power. The evolution of n parallels the divergence of wing shape between hawkmoths and silkmoths. High n may be the key to conducting high speed maneuvers in small flapping flyers like hawkmoths. Although hawkmoths have not evolved forewing shapes thought to be advantageous for maneuverability, it is clear that hawkmoths have evolved a means to accomplish rapid maneuvers while foraging (Wasserthal, 1993; Sponberg et al., 2015; Stöckl et al., 2017a). As opposed to fixed-wing cases, maneuverability of flapping flight relies on the generation of aerodynamic forces from wing movement to initiate directional change (Warrick et al., 1998).Therefore, an increase in n would allow for more frequent modification of force vectors, which could increase maneuverability. Further, increasing n will also enhance maneuverability by increasing the force and torque produced by a wing of similar shape and area (Hedrick et al., 2009), which is also exemplified in Model 3 of this study (Fig. 5C). The diversification of n could therefore contribute to interspecific variation in flight control and maneuverability across species. Although n was inferred from

scaling in this study, the estimate closely matches the observed frequency of the species considered here that have a known n. To the best that we can assess, n has strongly diverged between hawkmoths and silkmoths, and mean n is nearly double for a hawkmoth in comparison to a silkmoth of similar body size (Table 1, 2). Therefore, we suggest that high n is one of the aspects of flight control that evolved in hawkmoths allowing for the completion of high frequency maneuvers while employing wings of high AR, W_s, and $\hat{r}_2$.

Two strategies for agile flight. Silkmoths and hawkmoths have evolved two distinct strategies for agile flapping flight. Species of both families have evolved mechanisms for maneuverability and power reduction, but have distinctly different wing shapes. Hawkmoths achieve maneuverability through high n (movement) and reduce power by employing wings of high AR (shape), while silkmoths achieve maneuverability through favorable wing shapes and a reduction of power through the production of high amplitude wing strokes. The evolutionary trajectories of forewing shape have diverged between the two families, but the distinct flight strategies arise in part due to how differently they use their wings. The metrics of forewing shape, historically derived for fixed-winged aircraft, are not consistent with initial expectations of flight maneuverability based on the life history of species in each clade. Instead, we find that aerodynamic performance emerges from the interaction of wing shape, size, and movement (kinematics), demonstrating an example of parallel evolution between the components of a complex locomotor system (Aiello et al., 2017). The ability for natural selection to act both on wing shape and movement to impact the power requirements and maneuverability of an animal demonstrates the potential decoupling of animal locomotor performance metrics. The employment of flapping flight therefore provides the flexibility to tune aerodynamics through kinematics. Thus, we suggest the complex interplay between wing shape, size, and movement in resultant performance reduces morphological constraints that would drive the convergent evolution of wings to meet one or few advantageous shapes, leading to the diversity of wing shapes seen across extant aerial animals.

ACKNOWLEDGMENTS

We thank Jesse Barber, Stephanie Gage, Jeff Gau, Megan Matthews, Izaak Neveln, David Plotkin, Joy Putney, Juliette Rubin, Varun Sharma, Ryan St Laurent, and Travis Tune for helpful discussions, Aaron Olsen for assistance with image digitization and analysis, Milton Tan, Talia Moore, and Sarah Friedman for advice on phylogenetic methods, Bo Cheng and Yagiz Bayiz for advice on the aerodynamic blade element model, and Laurel Kaminsky for assistance in imaging museum specimens.

FUNDING

This work was supported by the National Science Foundation under a Postdoctoral Research Fellowships in Biology DBI #1812107 to B.R.A., a Faculty Early Career Development Award #1554790 to S.S., and grants DBI #1349345, DEB #1557007, and IOS #1920895 to A.Y.K., and a Dunn Family Professorship to S.S.

APPENDIX

Table A.1. List of symbols in the alphabetical order.

Symbol	Definition
A.B.	ancient bombycoids
$\mathrm{AR} = R^2/S$	aspect ratio
$(a_{\phi,k}, b_{\phi,k})$	Fourier series coefficients of Fourier fits of ϕ
$(a_{\theta,k}, b_{\theta,k})$	Fourier series coefficients of Fourier fits of θ
$(a_{\alpha,k}, b_{\alpha,k})$	Fourier series coefficients of Fourier fits of α
$\hat{\boldsymbol{b}}$	trailing edge to leading edge unit vector
C_{D}	aerodynamic coefficient of the drag force
C_{L}	aerodynamic coefficient of the lift force
C_{R}	coefficient of the rotational aerodynamic force
c	chord length
$\bar{c}$	Mean chordwise wing length
d	distance between the wing-attached y-axis (wing-pitching axis) and the quarter-chord line on the wing
dr	width of an infinitesimal blade element strip
e	distance between the leading edge and the wing-pitching axis

Continuation of Table A.1	
Symbol	Definition
$\boldsymbol{f} = \begin{bmatrix} f_x \\ f_y \\ f_z \end{bmatrix}$	force vector
$\boldsymbol{f}_{\mathrm{tra}}$	translational aerodynamic force vector
$\boldsymbol{f}_{\mathrm{D}}$	drag component vector of the translational aerodynamic force
$\hat{\boldsymbol{f}}_{\mathrm{D}}$	drag component unit vector of the translational aerodynamic force
$\boldsymbol{f}_{\mathrm{L}}$	lift component vector of the translational aerodynamic force
$\hat{\boldsymbol{f}}_{\mathrm{L}}$	lift component unit vector of the translational aerodynamic force
$\boldsymbol{f}_{\mathrm{rot}}$	rotational aerodynamic force vector
$\boldsymbol{f}_{\mathrm{adm}}$	aerodynamic force vector due to the added mass
$\boldsymbol{f}_{\mathrm{right}}$	vector of the total aerodynamic force on right wing
h	distance between the wing-attached y-axis (wing-pitching axis) and the half-chord line on the wing
$\boldsymbol{I} = \begin{bmatrix} I_{xx} & -I_{xy} & -I_{xz} \\ -I_{xy} & I_{yy} & -I_{yz} \\ -I_{xz} & -I_{yz} & I_{zz} \end{bmatrix}$	body's moment of inertia tensor
$\boldsymbol{l}_1$	position vector from body center of mass to the wing hinge point
l_{b}	body length
l_{abd}	abdomen length
$\hat{l}_{\mathrm{abd}} = l_{\mathrm{abd}}/l_{\mathrm{b}}$	fraction of body length occupied by abdomen
$\hat{l}_{\mathrm{tho}} = l_{\mathrm{tho}}/l_{\mathrm{b}}$	fraction of body length occupied by thorax
MYA	million years ago
$\boldsymbol{M}_{\mathrm{tra}}$	translational aerodynamic moment pseudovector
$\boldsymbol{M}_{\mathrm{rot}}$	rotational aerodynamic moment pseudovector
$\boldsymbol{M}_{\mathrm{adm}}$	aerodynamic moment pseudovector due to added-mass force
$\boldsymbol{M}_{\mathrm{right}}$	total aerodynamic moment pseudovector of right wing
m_{b}	body mass
m_{w}	wing mass
$m_{\mathrm{t}} = m_{\mathrm{b}} + 2m_{\mathrm{w}}$	Total (body+wings) mass
n	wingbeat frequency

Continuation of Table A.1	
Symbol	Definition
$n = 187 m_{\mathrm{t}}^{0.3} S^{-0.7}$	wingbeat frequency
$\hat{\boldsymbol{n}}$	unit vector normal to the dorsal surface of the wing
$P_{\mathrm{pro}} = \frac{1}{T}\int_0^T \int_0^R \frac{1}{2} C_{\mathrm{D}} \rho c v^3 \; dr \; dt / m_{\mathrm{t}}$	body mass-specific mean profile power
$P_{\mathrm{ind}} = w\left(m_{\mathrm{t}} g - f_{\mathrm{D},z}\right)/m_{\mathrm{t}}$	body mass-specific mean induced power
$P_{\mathrm{acc}} = 8\pi^2 \phi_{\mathrm{p\text{-}p}}^2 n^2 R^2 \hat{r}_2 m_{\mathrm{w}} / m_{\mathrm{t}}$	body mass-specific mean inertial power
pPCn	n^{th} axis of the phylogenetic principal components
$\mathbf{R}_z(\phi)$	transformation matrix for rotation of ϕ radians about the z-axis
$\mathbf{R}_x(\theta)$	transformation matrix for rotation of θ radians about the x-axis
$\mathbf{R}_y(\beta)$	transformation matrix for rotation of β radians about the y-axis
$\mathbf{R}_{\mathrm{w}}^{\mathrm{b}}$	transformation matrix for rotating the coordinate system from wing-attached to body-attached frame
R	spanwise wing length
$\boldsymbol{r}_{\mathrm{cm}}$	position vector from the body center of mass to a blade element strip of the wing
$\boldsymbol{r}_{\mathrm{wh}}$	position vector from the wing hinge to a blade element strip of the wing
r	distance of a blade element wing strip from the wing hinge along the y^{w} axis
$\boldsymbol{r}_3$	position vector from body center of mass to the quarter-chord line on a blade-element wing strip
$\boldsymbol{r}_1$	position vector from body center of mass to the half-chord line on a blade-element wing strip
$\hat{r}_2 = \sqrt{\int_0^1 \hat{c}\; \hat{r}^2 d\hat{r}}$	nondimensional radius of second moment of area
S	wing area
$T = 1/n$	wingbeat time period
t	time variable during a wingstroke, where $t = 0$ corresponds to the start of the downstroke
v	relative airflow speed
$\boldsymbol{v}$	relative airflow velocity vector
$\hat{\boldsymbol{v}}$	relative airflow velocity unit vector
$\boldsymbol{v}_{\mathrm{b}}$	body linear velocity vector

Continuation of Table A.1	
Symbol	Definition
$W_\mathrm{s} = m_\mathrm{t}/S$	wing loading
w_0	induced airflow speed
$x^\mathrm{b}y^\mathrm{b}z^\mathrm{b}$	body-attached coordinate frame
$x^l y^l z^l$	body-long coordinate frame
$x^\mathrm{sp}y^\mathrm{sp}z^\mathrm{sp}$	stroke-plane coordinate frame
$x^\mathrm{w}y^\mathrm{w}z^\mathrm{w}$	wing-attached coordinate frame
$\hat{\boldsymbol{y}}^\mathrm{w}$	unit vector along the wing-attached y-axis (wing-pitching axis)
α	wing pitching angle (feathering angle)
$\dot{\alpha}$	wing pitching angular velocity
$\alpha_\text{p-p}$	peak-to-peak amplitude of the feathering angle
$\overline{\alpha}$	mean feathering angle
α_e	effective angle of attack
α_r	effective angle of attack bound between 0 and 90°
β	stroke-plane angle
θ	stroke deviation angle
$\dot{\theta}$	stroke deviation angular velocity
$\theta_\text{p-p}$	peak-to-peak deviation angle
$\overline{\theta}$	mean deviation angle
ρ	density of air
ϕ	stroke positional angle (sweep angle)
$\dot{\phi}$	stroke positional angular velocity
$\phi_\text{p-p}$	peak-to-peak amplitude of the stroke positional (sweep) angle
$\overline{\phi}$	mean sweep angle
χ	body angle
χ_1	angle of inclination of the wing hinge from the center of mass with respect to the body-long xy-plane
χ_e	angle of inclination of the wing hinge from the center of mass with respect to the horizontal plane
$\boldsymbol{\omega}_\mathrm{w}$	wing angular velocity pseudovector due to wing kinematic motion
$\boldsymbol{\omega}_\mathrm{b}$	body angular velocity pseudovector

Continuation of Table A.1	
Symbol	Definition
Superscripts:	
b	measured with respect to the body-attached coordinate frame
l	measured with respect to the body-long frame
sp	measured with respect to the stroke-plane frame
w	measured with respect to the wing-attached coordinate frame

REFERENCES

Ahmad, A. (1984). A comparative study on flight surface and aerodynamic parameters of insects, birds and bats. *Indian J Exp Biol* **22**, 270–278.

Aiello, B. R., Westneat, M. W. and Hale, M. E. (2017). Mechanosensation is evolutionarily tuned to locomotor mechanics. *Proc Natl Acad Sci U S A* **14**, 4459–4464.

Aldridge, H. D. J. N. (1987). Turning Flight of Bats. *Journal of Experimental Biology* **128**, 419–425.

Baliga, V. B., Szabo, I. and Altshuler, D. L. (2019). Range of motion in the avian wing is strongly associated with flight behavior and body mass. *Science Advances* **5**.

Barber, J. R., Leavell, B. C., Keener, A. L., Breinholt, J. W., Chadwell, B. A., McClure, C. J. W., Hill, G. M. and Kawahara, A. Y. (2015). Moth tails divert bat attack: Evolution of acoustic deflection. *Proceedings of the National Academy of Sciences of the United States of America* **112**, 2812–2816.

Berman, G. J. and Wang, Z. J. (2007). Energy-minimizing kinematics in hovering insect flight. *Journal of Fluid Mechanics* **582**, 153–168.

Berwaerts, K., Van Dyck, H. and Aerts, P. (2002). Does flight morphology relate to flight performance? An experimental test with the butterfly Pararge aegeria. *Functional Ecology* **16**, 484–491.

Betts, C. R. and Wootton, R. J. (1988). Wing Shape and Flight Behavior in Butterflies (Lepidoptera, Papilionoidea and Hesperioidea) - a Preliminary-Analysis. *Journal of Experimental Biology* **138**, 271–288.

Breinholt, J. W., Earl, C., Lemmon, A. R., Lemmon, E. M., Xiao, L. and Kawahara, A. Y. (2018). Resolving Relationships among the Megadiverse Butterflies and Moths with a Novel Pipeline for Anchored Phylogenomics. *Systematic Biology* **67**, 78–93.

Burns, J. G. and Ydenberg, R. C. (2002). The effects of wing loading and gender on the escape flights of least sandpipers (Calidris minutilla) and western sandpipers (Calidris mauri). *Behavioral Ecology and Sociobiology* **52**, 128–136.

Byrne, D. N., Buchmann, S. L. and Spangler, H. G. (1988). Relationship between Wing Loading, Wingbeat Frequency and Body-Mass in Homopterous Insects. *Journal of Experimental Biology* **135**, 9–23.

Callahan, P. S. (1965). A Photoelectric-Photographic Analysis of Flight Behavior in the Corn Earworm, Heliothis sea, and Other Moths. *Annals of the Entomological Society of America* **58**, 159–169.

Cespedes, A., Penz, C. M. and DeVries, P. J. (2015). Cruising the rain forest floor: butterfly wing shape evolution and gliding in ground effect. *Journal of Animal Ecology* **84**, 808–816.

Cheng, B., Deng, X. Y. and Hedrick, T. L. (2011). The mechanics and control of pitching manoeuvres in a freely flying hawkmoth (Manduca sexta). *Journal of Experimental Biology* **214**, 4092–4106.

Cheng, B., Tobalske, B. W., Powers, D. R., Hedrick, T. L., Wang, Y., Wethington, S. M., Chiu, G. T. C. and Deng, X. Y. (2016a). Flight mechanics and control of escape manoeuvres in hummingbirds. II. Aerodynamic force production, flight control and performance limitations. *Journal of Experimental Biology* **219**, 3532–3543.

Cheng, B., Tobalske, B. W., Powers, D. R., Hedrick, T. L., Wethington, S. M., Chiu, G. T. C. and Deng, X. Y. (2016b). Flight mechanics and control of escape manoeuvres in hummingbirds. I. Flight kinematics. *Journal of Experimental Biology* **219**, 3518–3531.

Cho, S., Epstein, S. W., Mitter, K., Hamilton, C. A., Plotkin, D., Mitter, C. and Kawahara, A. Y. (2016). Preserving and vouchering butterflies and moths for large-scale museum-based molecular research. *Peerj* **4**.

Crandell, K. E. and Tobalske, B. W. (2011). Aerodynamics of tip-reversal upstroke in a revolving pigeon wing. *Journal of Experimental Biology* **214**, 1867–1873.

Dakin, R., Segre, P. S., Straw, A. D. and Altshuler, D. L. (2018). Morphology, muscle capacity, skill, and maneuvering ability in hummingbirds. *Science* **359**, 653–657.

Deakin, M. A. B. (2010). Formulae for insect wingbeat frequency. *Journal of Insect Science* **10**.

DeVries, P. J., Penz, C. M. and Hill, R. I. (2010). Vertical distribution, flight behaviour and evolution of wing morphology in Morpho butterflies. *Journal of Animal Ecology* **79**, 1077–1085.

Dudley, R. (2000). *The biomechanics of insect flight : form, function, evolution.* Princeton University Press, 476 pp.

Dudley, R. (2002). Mechanisms and implications of animal flight maneuverability. *Integr Comp Biol* **42**, 135–140.

Dudley, R. and Srygley, R. B. (1994). Plight Physiology of Neotropical Butterflies - Allometry of Airspeeds during Natural Free-Flight. *Journal of Experimental Biology* **191**, 125–139.

Ellington, C. P. (1984a). The Aerodynamics of Hovering Insect Flight .2. Morphological Parameters. *Philosophical Transactions of the Royal Society of London Series B-Biological Sciences* **305**, 17–40.

Ellington, C. P. (1984b). The Aerodynamics of Hovering Insect Flight 4. Aerodynamic Mechanisms. *Philosophical Transactions of the Royal Society of London Series B-Biological Sciences* **305**, 41–78.

Ellington, C. P. (1984c). The Aerodynamics of Hovering Insect Flight 6. Lift and Power Requirements. *Philosophical Transactions of the Royal Society of London Series B-Biological Sciences* **305**, 145–181.

Ellington, C. P., VandenBerg, C., Willmott, A. P. and Thomas, A. L. R. (1996). Leading-edge vortices in insect flight. *Nature* **384**, 626–630.

Etkin, B. and Reid, L. D. (1996). *Dynamics of flight: stability and control.* New York: Wiley, third edition edition.

Farina, W. M., Varju, D. and Zhou, Y. (1994). The Regulation of Distance to Dummy Flowers during Hovering Flight in the Hawk Moth Macroglossum-Stellatarum. *Journal of Comparative Physiology a-Sensory Neural and Behavioral Physiology* **174**, 239–247.

Faruque, I. and Humbert, J. S. (2010a). Dipteran insect flight dynamics. Part 1 Longitudinal motion about hover. *J Theor Biol* **264**, 538–552.

Faruque, I. and Humbert, J. S. (2010b). Dipteran insect flight dynamics. Part 2: Lateral-directional motion about hover. *J Theor Biol* **265**, 306–313.

Felsenstein, J. (1985). Phylogenies and the Comparative Method. *American Naturalist* **125**, 1–15.

Fernandez, M. J., Driver, M. E. and Hedrick, T. L. (2017). Asymmetry costs: effects of wing damage on hovering flight performance in the hawkmoth Manduca sexta. *Journal of Experimental Biology* **220**, 3649–3656.

Fung, Y. C. (1969). *An introduction to the theory of aeroelasticity.* New York: Dover.

Gage, S. L., Daly, K. C. and Nighorn, A. (2013). Nitric oxide affects short-term olfactory memory in the antennal lobe of Manduca sexta. *Journal of Experimental Biology* **216**, 3294–3300.

Gilchrist, G. W. (1990). The Consequences of Sexual Dimorphism in Body Size for Butterfly Flight and Thermoregulation. *Functional Ecology* **4**, 475–487.

Hamilton, C. A., St Laurent, R. A., Dexter, K., Kitching, I. J., Breinholt, J. W., Zwick, A., Timmermans, M., Barber, J. R. and Kawahara, A. Y. (2019). Phylogenomics resolves major relationships and reveals significant diversification rate shifts in the evolution of silk moths and relatives. *BMC Evol Biol* **19**, 182.

Han, J. S., Kim, J. K., Chang, J. W. and Han, J. H. (2015). An improved quasi-steady aerodynamic model for insect wings that considers movement of the center of pressure. *Bioinspiration and Biomimetics* **10**.

Hedenstrom, A. and Rosen, M. (2001). Predator versus prey: on aerial hunting and escape strategies in birds. *Behavioral Ecology* **12**, 150–156.

Hedrick, T. L., Cheng, B. and Deng, X. (2009). Wingbeat time and the scaling of passive rotational damping in flapping flight. *Science* **324**, 252–255.

Hedrick, T. L. and Daniel, T. L. (2006). Flight control in the hawkmoth Manduca sexta: the inverse problem of hovering. *Journal of Experimental Biology* **209**, 3114–3130.

Hildebrand, J. G. (1996). Olfactory control of behavior in moths: central processing of odor information and the functional significance of olfactory glomeruli. *Journal of Comparative Physiology a-Neuroethology Sensory Neural and Behavioral Physiology* **178**, 5–19.

Jacobs, D. S. and Bastian, A. (2016). *Predator-prey interactions: co-evolution between bats and their prey.* Cham, Switzerland: Springer.

Janzen, D. H. (1984). Two ways to be a tropical big moth: Santa Rosa saturniids and sphingids. In *Oxford surveys in evolutionary biology* (ed. D. R. R. M), pp. 85–140. Oxford: Oxford University Press.

Kawahara, A. Y. and Barber, J. R. (2015). Tempo and mode of antibat ultrasound production and sonar jamming in the diverse hawkmoth radiation. *Proceedings of the National Academy of Sciences of the United States of America* **112**, 6407–6412.

Kawahara, A. Y., Plotkin, D., Espeland, M., Meusemann, K., Toussaint, E. F. A., Donath, A., Gimnich, F., Frandsen, P. B., Zwick, A., dos Reis, M. et al. (2019). Phylogenomics reveals the evolutionary timing and pattern of butterflies and moths. *Proceedings of the National Academy of Sciences of the United States of America* **116**, 22657–22663.

Kim, J.-K. and Han, J.-H. (2014). A multibody approach for 6-DOF flight dynamics and stability analysis of the hawkmothManduca sexta. *Bioinspiration & Biomimetics* **9**, 16011.

Kim, J.-K., Han, J.-S., Lee, J.-S. and Han, J.-H. (2015). Hovering and forward flight of the hawkmoth *Manduca sexta*: trim search and 6-DOF dynamic stability characterization. *Bioinspiration & Biomimetics* **10**, 56012.

Kitching, I. J., Rougerie, R., Zwick, A., Hamilton, C. A., St Laurent, R. A., Naumann, S., Mejia, L. B. and Kawahara, A. Y. (2018). A global checklist of the Bombycoidea (Insecta: Lepidoptera). *Biodiversity Data Journal* **6**.

Knorlein, B. J., Baier, D. B., Gatesy, S. M., Laurence-Chasen, J. D. and Brainerd, E. L. (2016). Validation of XMALab software for marker-based XROMM. *Journal of Experimental Biology* **219**, 3701–3711.

Kueck, P. and Longo, G. C. (2014). FASconCAT-G: extensive functions for multiple sequence alignment preparations concerning phylogenetic studies. *Frontiers in Zoology* **11**.

Larsson, A. (2014). AliView: a fast and lightweight alignment viewer and editor for large datasets. *Bioinformatics* **30**, 3276–3278.

Le Roy, C., Debat, V. and Llaurens, V. (2019). Adaptive evolution of butterfly wing shape: from morphology to behaviour. *Biological Reviews* **94**, 1261–1281.

Lemaire, C. and Minet, J. (1998). The Bombycoidea and their relatives. In *Handbook of Zoology, Volume IV, Arthropoda: Insecta* (ed. N. P. Kristensen), pp. 321–353. Berlin: Walter de Gruyter.

Lemmon, A. R., Emme, S. A. and Lemmon, E. M. (2012). Anchored Hybrid Enrichment for Massively High-Throughput Phylogenomics. *Systematic Biology* **61**, 727–744.

Lentink, D., Muller, U. K., Stamhuis, E. J., de Kat, R., van Gestel, W., Veldhuis, L. L. M., Henningsson, P., Hedenstrom, A., Videler, J. J. and van Leeuwen, J. L. (2007). How swifts control their glide performance with morphing wings. *Nature* **446**, 1082–1085.

Lewis, F. P., Fullard, J. H. and Morrill, S. B. (1993). Auditory Influences on the Flight Behavior of Moths in a Nearctic Site .2. Flight Times, Heights, and Erraticism. *Canadian Journal of Zoology-Revue Canadienne De Zoologie* **71**, 1562–1568.

Matthews, M. and Sponberg, S. (2018). Hawkmoth flight in the unsteady wakes of flowers. *The Journal of Experimental Biology* **221**, jeb179259.

Maybury, W. J. and Lehmann, F.-O. (2004). The fluid dynamics of flight control by kinematic phase lag variation between two robotic insect wings. *Journal of Experimental Biology* **207**, 4707–4726.

Minh, B. Q., Nguyen, M. A. T. and von Haeseler, A. (2013). Ultrafast Approximation for Phylogenetic Bootstrap. *Molecular Biology and Evolution* **30**, 1188–1195.

Muijres, F. T., Iwasaki, N. A., Elzinga, M. J., Melis, J. M. and Dickinson, M. H. (2017). Flies compensate for unilateral wing damage through modular adjustments of wing and body kinematics. *Interface Focus* **7**.

Natesan, D., Saxena, N., Ekeberg, O. and Sane, S. P. (2019). Tuneable reflexes control antennal positioning in flying hawkmoths. *Nat Commun* **10**.

Nguyen, L. T., Schmidt, H. A., von Haeseler, A. and Minh, B. Q. (2015). IQ-TREE: A Fast and Effective Stochastic Algorithm for Estimating Maximum-Likelihood Phylogenies. *Molecular Biology and Evolution* **32**, 268–274.

Norberg, U. M. and Rayner, J. M. V. (1987). Ecological Morphology and Flight in Bats (Mammalia, Chiroptera) - Wing Adaptations, Flight Performance, Foraging Strategy and Echolocation. *Philosophical Transactions of the Royal Society B-Biological Sciences* **316**, 337–419.

Olsen, A. M. (2017). Feeding ecology is the primary driver of beak shape diversification in waterfowl. *Functional Ecology* **31**, 1985–1995.

Olsen, A. M. and Westneat, M. W. (2015). StereoMorph: an R package for the collection of 3D landmarks and curves using a stereo camera set-up. *Methods in Ecology and Evolution* **6**, 351–356.

Pennycuick, C. J. (1968). Power Requirements for Horizontal Flight in Pigeon Columba Livia. *Journal of Experimental Biology* **49**, 527–+.

Ray, R. P., Nakata, T., Henningsson, P. and Bomphrey, R. J. (2016). Enhanced flight performance by genetic manipulation of wing shape in Drosophila. *Nat Commun* **7**, 10851.

Revell, L. J. (2009). Size-Correction and Principal Components for Interspecific Comparative Studies. *Evolution* **63**, 3258–3268.

Revell, L. J. (2012). phytools: An R package for phylogenetic comparative biology (and other things). *Methods Ecol. Evol.* **3**, 217–223.

Riffell, J. A., Lei, H., Abrell, L. and Hildebrand, J. G. (2013). Neural basis of a pollinator's buffet: olfactory specialization and learning in Manduca sexta. *Science* **339**, 200–204.

Riskin, D. K., Iriarte-Diaz, J., Middleton, K. M., Breuer, K. S. and Swartz, S. M. (2010). The effect of body size on the wing movements of pteropodid bats, with insights into thrust and lift production. *Journal of Experimental Biology* **213**, 4110–4122.

Roth, E., Hall, R. W., Daniel, T. L. and Sponberg, S. (2016). Integration of parallel mechanosensory and visual pathways resolved through sensory conflict. *Proceedings of the National Academy of Sciences* **113**, 12832–12837.

Rubin, J. J., Hamilton, C. A., McClure, C. J. W., Chadwell, B. A., Kawahara, A. Y. and Barber, J. R. (2018). The evolution of anti-bat sensory illusions in moths. *Science Advances* **4**.

Sane, S. P. and Dickinson, M. H. (2001). The control of flight force by a flapping wing: lift and drag production. *The Journal of experimental biology* **204**, 2607–26.

Sane, S. P. and Dickinson, M. H. (2002). The aerodynamic effects of wing rotation and a revised quasi-steady model of flapping flight. *Journal of Experimental Biology* **205**, 1087–1096.

Sponberg, S., Dyhr, J. P., Hall, R. W. and Daniel, T. L. (2015). Luminance-dependent visual processing enables moth flight in low light. *Science* **348**, 1245–1248.

Sprayberry, J. D. H. and Daniel, T. L. (2007). Flower tracking in hawkmoths: behavior and energetics. *Journal of Experimental Biology* **210**, 37–45.

Stöckl, A. L., Kihlström, K., Chandler, S. and Sponberg, S. (2017a). Comparative system identification of flower tracking performance in three hawkmoth species reveals adaptations for dim light vision. *Philosophical Transactions of the Royal Society B-Biological Sciences* **372**, 20160078–20160079.

Stöckl, A. L., O'Carroll, D. and Warrant, E. J. (2017b). Higher-order neural processing tunes motion neurons to visual ecology in three species of hawkmoths. *Proceedings of the Royal Society B: Biological Sciences* **284**, 20170880.

Stowers, A. K., Matloff, L. Y. and Lentink, D. (2017). How pigeons couple three-dimensional elbow and wrist motion to morph their wings. *Journal of the Royal Society Interface* **14**.

Tammaru, T. and Haukioja, E. (1996). Capital breeders and income breeders among Lepidoptera - Consequences to population dynamics. *Oikos* **77**, 561–564.

Truong, Q. T., Nguyen, Q. V., Truong, V. T., Park, H. C., Byun, D. Y. and Goo, N. S. (2011). A modified blade element theory for estimation of forces generated by a beetle-mimicking flapping wing system. *Bioinspiration and Biomimetics* **6**.

Tuskes, P. M., Tuttle, J. P. and Collins, M. M. (1996). *The Wild Silk Moths of North America: A Natural History of the Saturniidae of the United States and Canada.* Ithica, NY: Cornell University Press.

Tuttle, J. (2007). The Hawk Moths of North America: A Natural History Study of the Sphingidae of the United States and Canada.

Usherwood, J. R. and Ellington, C. P. (2002). The aerodynamics of revolving wings II. Propeller force coefficients from mayfly to quail. *Journal of Experimental Biology* **205**, 1565–1576.

Warrick, D. R., Dial, K. P. and Biewener, A. A. (1998). Asymmetrical force production in the slow maneuvering flight of pigeons. *Auk* **115**, 916–928.

Wasserthal, L. (1993). Swing-hovering combined with long tongue in hawkmoths, an antipredator adaptation during flower visits. In *Animal-plant interactions in tropical environments.* (ed. B. W. N. C. S.-L. K. S. LL), pp. 77–87. Bonn: Zoologisches Forschungsinstitut und Museum König.

Wasserthal, L. T. (1998). Deep flowers for long tongues. *Trends in Ecology & Evolution* **13**, 459–460.

Willmott, A. P. and Ellington, C. P. (1997a). The mechanics of flight in the hawkmoth *Manduca sexta.* I. Kinematics of hovering and forward flight. *Journal of Experimental Biology* **200**, 2705–2722.

Willmott, A. P. and Ellington, C. P. (1997b). The mechanics of flight in the hawkmoth *Manduca sexta.* II. Aerodynamic consequences of kinematic and morphological variation. *Journal of Experimental Biology* **200**, 2723–2745.

Windsor, S. P., Bomphrey, R. J. and Taylor, G. K. (2014). Vision-based flight control in the hawkmoth Hyles lineata. *Journal of the Royal Society Interface* **11**.

Wootton, R. J. (1992). Functional-Morphology of Insect Wings. *Annual Review of Entomology* **37**, 113–140.

Xia, Q. Y., Zhou, Z. Y., Lu, C., Cheng, D. J., Dai, F. Y., Li, B., Zhao, P., Zha, X. F., Cheng, T. C., Chai, C. L. et al. (2004). A draft sequence for the genome of the domesticated silkworm (Bombyx mori). *Science* **306**, 1937–1940.

Supplemental Information

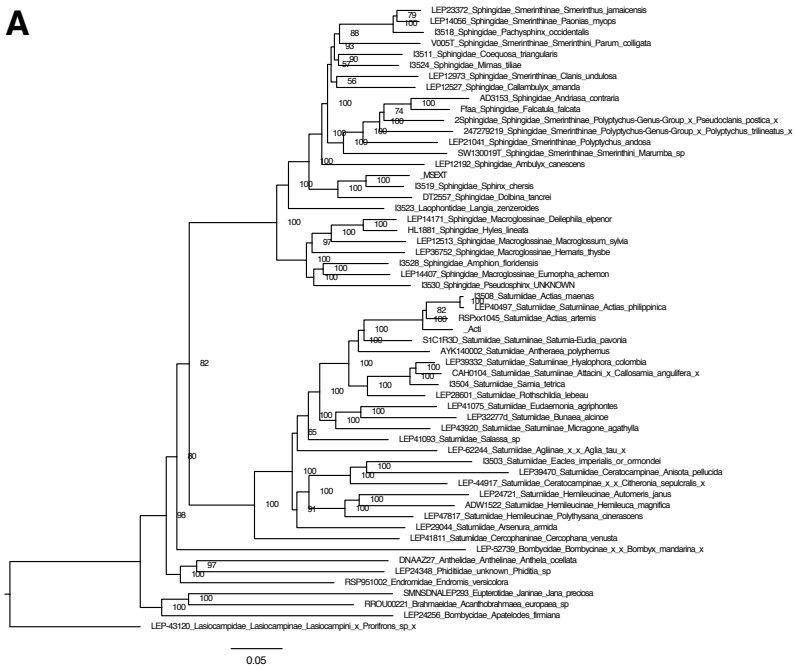

Fig. S1. **A** Bombycoid phylogeny with bootstrap values for each node. The values at each node represent the bootstrap support. **B** Key for phylogeny node labels. Numeric labels for each node of the phylogeny are listed in their corresponding location and housed within a blue box.

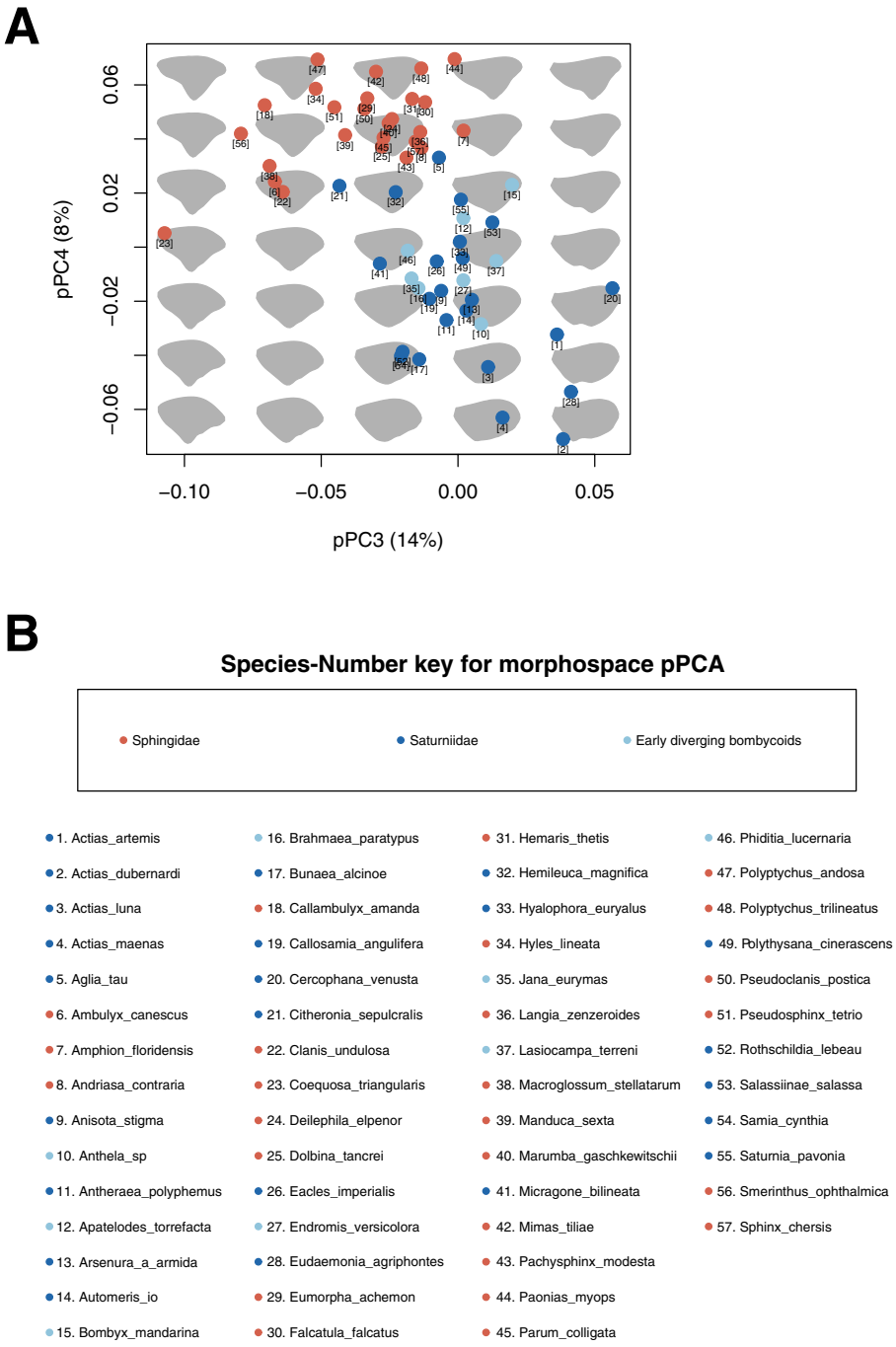

Fig. S2. **A** Forewing morphospace across the pPC3 and pPC4 axes. Projections of the taxa onto the third and fourth phylogenetic principal components also demonstrates the separation of extant hawkmoths and silkmoths. **B** Key for species names in morphospace. This figure contains the number and corresponding scientific name of each species in morphospace. These numbers are used in panel A and in Fig. 2

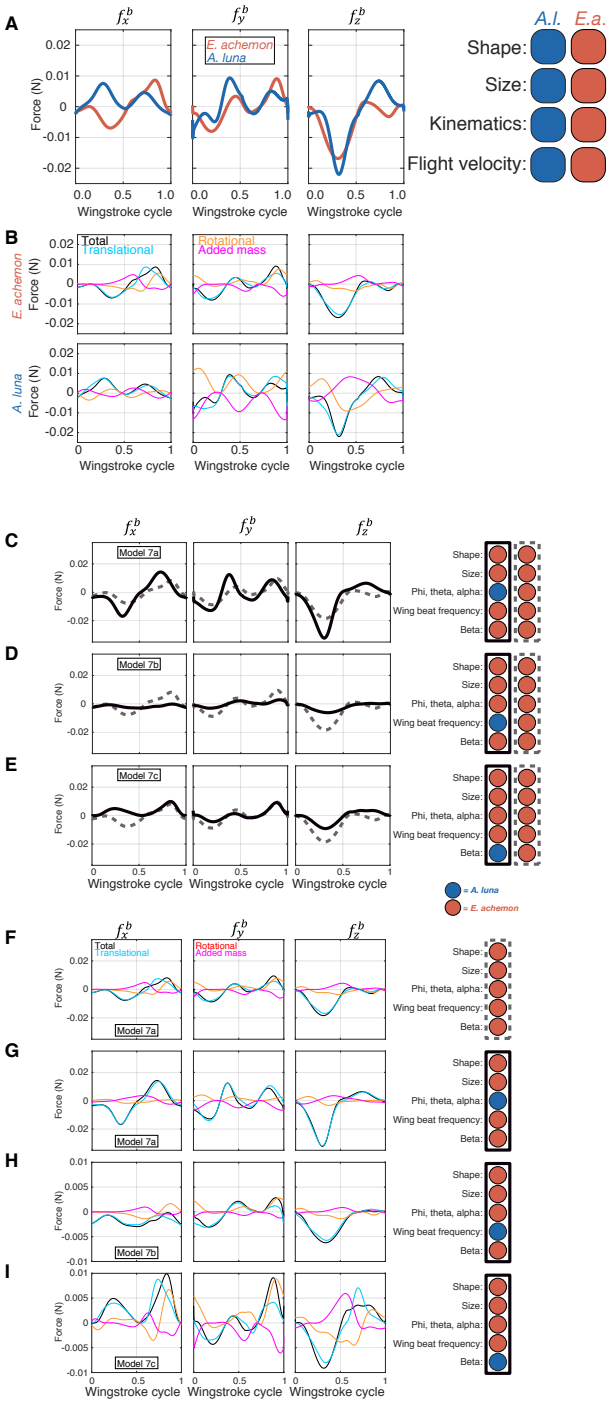

Fig. S3. A-B The total, translational, rotational, and added mass components of aerodynamic force during recoded flight speeds. (A) The total forces for *A. luna* (blue) and *E. achemon* (red) modeled at their natural flight velocities. (B) The component forces for each model using recorded flight velocities of each species. **C-I** The role of kinematic parameters in shaping the aerodynamics of each species. This set of models investigates the contribution of wing kinematics (C), wing beat frequency (D), and stroke plane angle (E) to total aerodynamic force production. In each panel, the two models are distinguished by solid and dashed lines. The variables used in each model can be found to the right of the data and are outlined in a corresponding solid or dashed line. The color of each circle represents the species from which each variable was measured. The components of the total aerodynamic force generated in each model are presented in panels **F-I**. The component forces for the dashed line model are only presented once (Panel E) because they are the same in each model.

Tip Name	Family	Genus	Species	Data	Dataset	Recovery	Geuns_species_of_imaged_moth	N Females	N Males	N Total
_Acti	Saturniidae	Actias	luna	transcriptome	Kawahara & Breinholt 2014	776	Actias_luna	0	2	2
_MSEXT	Sphingidae	Manduca	sexta	transcriptome	Kawahara & Breinholt 2014	790	Manduca_sexta	0	2	2
247279219_Sphingidae_Smerinthinae_Polyptychus-Genus-Group_x_Polyptychus_trilineatus_x	Sphingidae	Polyptychus	trilineatus	AHE	NEW	244	Polyptychus_trilineatus	0	2	2
2Sphingidae_Sphingidae_Smerinthinae_Polyptychus-Genus-Group_x_Pseudoclanis_postica_x	Sphingidae	Pseudoclanis	postica	AHE	NEW	496	Pseudoclanis_postica	0	2	2
AD3153_Sphingidae_Andriasa_contraria	Sphingidae	Andriasa	contraria	AHE	Hamilton et al., 2019	720	Andriasa_contraria	0	2	2
ADW1522_Saturniidae_Hemileucinae_Hemileuca_magnifica	Saturniidae	Hemileuca	magnifica	AHE	Hamilton et al., 2019	402	Hemileuca_magnifica	0	3	3
AYK140002_Saturniidae_Antheraea_polyphemus	Saturniidae	Antheraea	polyphemus	AHE	Rubin & Hamilton et al., 2018	750	Antheraea_polyphemus	0	5	5
CAH0104_Saturniidae_Saturniinae_Attacini_x_Callosamia_angulifera_x	Saturniidae	Callosamia	angulifera	AHE	NEW	564	Callosamia_angulifera	0	5	5
DNAAZ27_Anthelidae_Anthelinae_Anthela_ocellata	Anthelidae	Anthela	ocellata	AHE	Hamilton et al., 2019	442	Anthela_sp	1	0	1
DT2557_Sphingidae_Dolbina_tancrei	Sphingidae	Dolbina	tancrei	AHE	Hamilton et al., 2019	774	Dolbina_tancrei	0	2	2
Ffaa_Sphingidae_Falcatula_falcata	Sphingidae	Falcatula	falcata	AHE	Hamilton et al., 2019	761	Falcatula_falcatus	0	1	1
HL1881_Sphingidae_Hyles_lineata	Sphingidae	Hyles	lineata	AHE	NEW	761	Hyles_lineata	0	2	2
I3503_Saturniidae_Eacles_imperialis_or_ormondei	Saturniidae	Eacles	imperialis	AHE	Hamilton et al., 2019	738	Eacles_imperialis	0	3	3
I3504_Saturniidae_Samia_tetrica	Saturniidae	Samia	tetrica	AHE	Rubin & Hamilton et al., 2018	753	Samia_cynthia	0	5	5
I3508_Saturniidae_Actias_maenas	Saturniidae	Actias	maenas	AHE	Rubin & Hamilton et al., 2018	766	Actias_maenas	0	2	2
I3511_Sphingidae_Coequosa_triangularis	Sphingidae	Coequosa	triangularis	AHE	Hamilton et al., 2019	766	Coequosa_triangularis	1	0	1
I3518_Sphingidae_Pachysphinx_occidentalis	Sphingidae	Pachysphinx	imperator	AHE	NEW	776	Pachysphinx_modesta	0	3	3
I3519_Sphingidae_Sphinx_chersis	Sphingidae	Sphinx	chersis	AHE	Hamilton et al., 2019	775	Sphinx_chersis	0	2	2
I3523_Laophontidae_Langia_zenzeroides	Sphingidae	Langia	zenzeroides	AHE	Hamilton et al., 2019	763	Langia_zenzeroides	0	2	2
I3524_Sphingidae_Mimas_tiliae	Sphingidae	Mimas	tiliae	AHE	NEW	780	Mimas_tiliae	0	2	2
I3528_Sphingidae_Amphion_floridensis	Sphingidae	Amphion	floridensis	AHE	NEW	766	Amphion_floridensis	0	2	2
I3530_Sphingidae_Pseudosphinx_UNKNOWN	Sphingidae	Pseudosphinx	tetrio	AHE	Hamilton et al., 2019	771	Pseudosphinx_tetrio	0	2	2
LEP-43120_Lasiocampidae_Lasiocampinae_Lasiocampini_x_Prorifrons_sp_x	Lasiocampidae	Prorifrons	sp	AHE	NEW	497	Lasiocampa_terreni	0	2	2
LEP-44917_Saturniidae_Ceratocampinae_x_x_Citheronia_sepulcralis_x	Saturniidae	Citheronia	sepulcralis	AHE	NEW	567	Citheronia_sepulcralis	0	2	2
LEP-52739_Bombycidae_Bombycinae_x_x_Bombyx_mandarina_x	Bombycidae	Bombyx	mandarina	AHE	NEW	586	Bombyx_mandarina	0	2	2
LEP-62244_Saturniidae_Agliinae_x_x_Aglia_tau_x	Saturniidae	Aglia	tau	AHE	NEW	565	Aglia_tau	0	3	3
LEP12192_Sphingidae_Ambulyx_canescens	Sphingidae	Ambulyx	canescens	AHE	Hamilton et al., 2019	723	Ambulyx_canescus	0	2	2
LEP12513_Sphingidae_Macroglossinae_Macroglossum_sylvia	Sphingidae	Macroglossum	sylvia	AHE	Hamilton et al., 2019	532	Macroglossum_stellatarum	0	1	1
LEP12527_Sphingidae_Callambulyx_amanda	Sphingidae	Callambulyx	amanda	AHE	Hamilton et al., 2019	741	Callambulyx_amanda	0	1	1
LEP12973_Sphingidae_Smerinthinae_Clanis_undulosa	Sphingidae	Clanis	undulosa	AHE	Hamilton et al., 2019	595	Clanis_undulosa	0	2	2
LEP14056_Sphingidae_Smerinthinae_Paonias_myops	Saturniidae	Paonias	myops	AHE	NEW	618	Paonias_myops	0	3	3
LEP14171_Sphingidae_Macroglossinae_Deilephila_elpenor	Sphingidae	Deilephila	elpenor	AHE	NEW	589	Deilephila_elpenor	0	2	2
LEP14407_Sphingidae_Macroglossinae_Eumorpha_achemon	Saturniidae	Eumorpha	achemon	AHE	NEW	597	Eumorpha_achemon	0	2	2
LEP21041_Sphingidae_Smerinthinae_Polyptychus_andosa	Sphingidae	Polyptychus	andosa	AHE	Hamilton et al., 2019	548	Polyptychus_andosa	0	2	2
LEP23372_Sphingidae_Smerinthinae_Smerinthus_jamaicensis	Sphingidae	Smerinthus	jamaicensis	AHE	Hamilton et al., 2019	605	Smerinthus_ophthalmica	2	0	2
LEP24256_Bombycidae_Apatelodes_firmiana	Apatelodidae	Apatelodes	firmiana	AHE	Hamilton et al., 2019	703	Apatelodes_torrefacta	0	3	3
LEP24348_Phiditiidae_unknown_Phiditia_sp	Phiditiidae	Phiditia	sp	AHE	NEW	547	Phiditia_lucernaria	0	2	2
LEP24721_Saturniidae_Hemileucinae_Automeris_janus	Saturniidae	Automeris	janus	AHE	NEW	614	Automeris_io	0	2	2
LEP28601_Saturniidae_Rothschildia_lebeau	Saturniidae	Rothschildia	lebeau	AHE	Rubin & Hamilton et al., 2018	533	Rothschildia_lebeau	0	4	4
LEP29044_Saturniidae_Arsenura_armida	Saturniidae	Arsenura	armida	AHE	Rubin & Hamilton et al., 2018	766	Arsenura_a_armida	0	3	3
LEP32277d_Saturniidae_Bunaea_alcinoe	Saturniidae	Bunaea	alcinoe	AHE	Rubin & Hamilton et al., 2018	702	Bunaea_alcinoe	0	2	2
LEP36752_Sphingidae_Macroglossinae_Hemaris_thysbe	Sphingidae	Hemaris	thysbe	AHE	Hamilton et al., 2019	592	Hemaris_thetis	0	1	1
LEP39332_Saturniidae_Saturniinae_Hyalophora_colombia	Saturniidae	Hyalophora	colombia	AHE	NEW	542	Hyalophora_euryalus	0	3	3
LEP39470_Saturniidae_Ceratocampinae_Anisota_pellucida	Saturniidae	Anisota	pellucida	AHE	Hamilton et al., 2019	585	Anisota_stigma	1	0	1
LEP40497_Saturniidae_Saturniinae_Actias_philippinica	Saturniidae	Actias	philippinica	AHE	Rubin & Hamilton et al., 2018	570	Actias_dubernardi	0	2	2
LEP41075_Saturniidae_Eudaemonia_agriphontes	Saturniidae	Eudaemonia	agriphontes	AHE	Rubin & Hamilton et al., 2018	760	Eudaemonia_agriphontes	0	3	3
LEP41093_Saturniidae_Salassa_sp	Saturniidae	Salassa	sp	AHE	Rubin & Hamilton et al., 2018	748	Salassiinae_salassa	0	3	3
LEP41811_Saturniidae_Cercophaninae_Cercophana_venusta	Saturniidae	Cercophana	venusta	AHE	Hamilton et al., 2019	598	Cercophana_venusta	0	2	2
LEP43920_Saturniidae_Saturniinae_Micragone_agathylla	Saturniidae	Micragone	agathylla	AHE	Rubin & Hamilton et al., 2018	561	Micragone_bilineata	0	1	1
LEP47817_Saturniidae_Hemileucinae_Polythysana_cinerascens	Saturniidae	Polythysana	cinerascens	AHE	Hamilton et al., 2019	525	Polythysana_cinerascens	0	2	2
RROU00221_Brahmaeidae_Acanthobrahmaea_europaea_sp	Brahmaeidae	Brahmaea	europaea	AHE	Hamilton et al., 2019	502	Brahmaea_paratypus	0	1	1
RSP951002_Endromidae_Endromis_versicolora	Endromidae	Endromis	versicolora	AHE	Hamilton et al., 2019	769	Endromis_versicolora	0	2	2
RSPxx1045_Saturniidae_Actias_artemis	Saturniidae	Actias	artemis	AHE	Rubin & Hamilton et al., 2018	764	Actias_artemis	0	2	2
S1C1R3D_Saturniidae_Saturniinae_Saturnia-Eudia_pavonia	Saturniidae	Saturnia	pavonia	AHE	Hamilton et al., 2019	588	Saturnia_pavonia	0	3	3
SMNSDNALEP293_Eupterotidae_Janinae_Jana_preciosa	Eupterotidae	Jana	preciosa	AHE	Hamilton et al., 2019	575	Jana_eurymas	0	2	2
SW130019T_Sphingidae_Smerinthinae_Smerinthini_Marumba_sp	Sphingidae	Marumba	sp	transcriptome	NEW	719	Marumba_gaschkewitschii	0	2	2
V005T_Sphingidae_Smerinthinae_Smerinthini_Parum_colligata	Sphingidae	Parum	colligata	transcriptome	NEW	723	Parum_colligata	0	2	2

Table S1. Tip names and data source of each species in phylogeny as well as sex and count of individuals used in shape analysis for each species

	All clades				Silkmoths and Hawkmoths only				Silkmoths only				Hawkmoths only			
VARIABLE	**Lambda**	**logL**	**logL0**	***p***	**Lambda**	**logL**	**logL0**	***p***	**Lambda**	**logL**	**logL0**	***p***	**Lambda**	**logL**	**logL0**	***p***
Wing length	6.73E−01	154.77413	152.72192	4.28E−02	5.97E−01	134.6286	132.7487	5.25E−02	4.78E−01	62.89071	62.43487	0.339669	7.53E−01	72.96265	72.68433	0.455618
Mean chord length of wing	8.04E−01	222.56847	211.63032	2.91E−06	7.17E−01	193.8313	182.1356	**1.32E−06**	5.92E−01	87.87921	86.95188	0.173243	2.23E−01	109.5684	109.4971	0.705753
Wing Area	6.61E−01	355.15542	349.67178	9.27E−04	5.76E−01	306.6241	300.5873	**5.11E−04**	3.86E−01	139.564	139.2045	0.396474	5.63E−01	171.762	171.774	1
Radius of second moment of area	8.94E−01	156.6572	146.81576	9.14E−06	7.62E−01	139.3126	133.2992	**5.24E−04**	7.98E−01	61.96275	60.67493	0.10852	7.95E−05	82.46353	82.46368	1
Aspect ratio	8.66E−01	−27.37978	−54.46312	1.84E−13	7.94E−01	−21.4874	−45.943	**2.68E−12**	6.70E−05	−3.61346	−3.61313	1	7.95E−05	−8.13094	−8.1307	1
Body length	4.93E−01	182.05982	180.31661	6.19E−02	3.30E−01	157.8792	155.8999	**4.66E−02**	6.70E−05	80.09822	80.09846	1	9.94E−01	81.85932	81.88774	1
Body mass	6.65E−05	−88.65496	−88.6541	1.00E+00	6.67E−05	−77.504	−77.5037	1.00E+00	6.70E−05	−28.0873	−28.0871	1	8.98E−01	−45.8953	−45.4909	1
Wing beat frequency	9.68E−01	−202.68686	−221.00342	1.43E−09	9.63E−01	−171.949	−191.554	**3.81E−10**	8.88E−01	−68.9056	−71.6001	**0.020265**	9.00E−01	−95.5285	−99.2592	**0.006303**
Wing loading	9.25E−01	88.49541	73.49837	4.33E−08	1.01E+00	77.64915	60.71952	**5.92E−09**	9.89E−01	55.15641	53.3409	0.056712	8.01E−01	35.38334	32.86191	**0.024728**
Thorax length (% body length)	7.41E−01	109.0667	103.55681	9.01E−04	4.11E−01	99.19072	93.71724	**9.38E−04**	5.95E−05	46.63365	46.63371	1	7.95E−05	55.46341	55.46362	1
Abdomen length (% body length)	8.02E−01	101.83411	97.28912	2.57E−03	5.92E−01	91.86848	88.17052	**6.54E−03**	4.29E−01	41.57689	41.19002	0.379065	7.25E−01	52.01277	50.48391	0.080354
Abdomen length (meters)	7.67E−01	202.6083	200.03252	2.32E−02	8.76E−01	176.1017	172.9968	**1.27E−02**	6.70E−05	88.18174	88.18192	1	9.23E−01	91.28054	91.34096	1
Inertial power	7.88E−01	−220.16556	−222.89423	1.95E−02	7.70E−01	−187.489	−188.932	8.93E−02	1.79E−01	−81.3109	−81.3337	0.830876	8.72E−01	−101.994	−103.019	0.152355
pPC1	7.92E−01	98.08059	73.38695	2.10E−12	7.23E−01	85.00891	61.67966	**8.45E−12**	6.70E−05	41.22814	41.22848	1	2.42E−01	54.4627	54.26087	0.525214
pPC2	6.41E−01	110.485	106.707	5.98E−03	8.20E−02	99.33557	99.25253	6.84E−01	3.04E−01	43.16479	42.8051	0.396353	7.95E−05	59.07206	59.07238	1
pPC3	5.89E−01	126.1117	118.483	9.38E−05	5.77E−01	107.7102	99.98249	**8.45E−05**	7.99E−01	54.79132	53.60685	0.123771	7.95E−05	57.79694	57.79727	1
pPC4	8.62E−01	133.768	107.5375	4.39E−13	8.49E−01	115.9159	90.28858	**8.11E−13**	7.81E−01	51.58913	50.12487	0.087028	7.95E−05	72.31542	72.31576	1

Significant *P* values are in bold

Table S2. Phylogenetic signal for each variable using the entire phylogeny and various pruned phylogenies

	pPC1			pPC2			Wing length			Mean chord length of wing			Wing area			Radius of the second moment of area			Aspect ratio			Body length		
Node number	Ancestral state	Upper 95% CI	Lower 95% CI	Ancestral state	Upper 95% CI	Lower 95% CI	Ancestral state	Upper 95% CI	Lower 95% CI	Ancestral state	Upper 95% CI	Lower 95% CI	Ancestral state	Upper 95% CI	Lower 95% CI	Ancestral state	Upper 95% CI	Lower 95% CI	Ancestral state	Upper 95% CI	Lower 95% CI	Ancestral state	Upper 95% CI	Lower 95% CI
58	-5.67E-16	-0.11478617	0.11478362	-0.11478617	-0.08438098	0.08438098	0.03530532	-0.00562559	0.07623623	0.01248199	-0.00133569	0.02629967	0.000524736	-1.03E-03	0.002078331	0.585369	0.5471965	0.6235415	2.848957	2.033795	3.664119	0.02829903	0.00343255	0.0531655
59	-2.56E-03	-0.0673881	0.06227856	-0.0673881	-0.06372247	0.03160684	0.03843712	0.015316293	0.06155795	0.01242219	0.005436965	0.02104747	0.000609192	-2.68E-04	0.001486778	0.574515	0.5529524	0.5960777	2.953081	2.492617	3.413545	0.02934259	0.01529615	0.04338902
60	-4.93E-03	-0.06152457	0.05166901	-0.06152457	-0.06647971	0.01673234	0.03754315	0.017361202	0.0577251	0.01262899	0.005721457	0.01932345	0.000561362	-2.05E-04	0.001237399	0.5689185	0.5500966	0.6877403	3.029427	2.627493	3.431362	0.02831734	0.01605633	0.04057834
61	-7.75E-03	-0.064090637	0.04859222	-0.064090637	-0.07104259	0.011794048	0.03776706	0.017676165	0.05785796	0.012499847	0.005717452	0.01928224	0.000560794	-2.02E-04	0.001323375	0.5671469	0.54841	0.5858839	3.083352	2.683231	3.483474	0.02846948	0.0162638	0.04067517
62	-1.22E-02	-0.06881048	0.04446395	-0.06881048	-0.07473722	0.008534501	0.03887431	0.01867789	0.05907073	0.012638435	0.005820417	0.01945645	0.000580437	-1.86E-04	0.001347023	0.5659436	0.5471082	0.5847789	3.141861	2.739638	3.544084	0.02914303	0.01687324	0.04141283
63	8.65E-02	-0.13423549	-0.03885563	-0.134235498	-0.08310554	-0.012888337	0.0425127	0.02550645	0.05951815	0.011062137	0.00532121	0.01680106	0.000540471	-1.05E-04	0.001145954	0.568373	0.5525132	0.5842417	3.862847	3.524166	4.201528	0.03648822	0.02615677	0.04681966
64	-9.25E-02	-0.138663194	-0.04643063	-0.138663194	-0.08575808	-0.01795508	0.04500151	0.028556813	0.0614462	0.011453115	0.005901626	0.0170046	0.000580611	-4.36E-05	0.001204794	0.567345	0.5520086	0.5826815	3.930447	3.602941	4.257952	0.0379693	0.02797876	0.04795983
65	-9.69E-02	-0.13681156	-0.05697497	-0.13681156	-0.07999142	-0.021301098	0.04530894	0.031074403	0.05954348	0.011444204	0.006638831	0.0162495 8	0.000569982	2.97E-05	0.001110276	0.5671425	0.5538672	0.5804177	3.962204	3.678716	4.245693	0.03858273	0.02993492	0.04723054
66	-9.64E-02	-0.131761302	-0.06106687	-0.131761302	-0.07612637	-0.024156717	0.0460027	0.03339817	0.05860723	0.011596277	0.00734117	0.01585138	0.000582517	1.04E-04	0.001060941	0.5662414	0.5544863	0.5779965	3.973969	3.722942	4.224995	0.03890117	0.03124363	0.04655872
67	-9.48E-02	-0.12786235	-0.06237826	-0.12786235	-0.07425989	-0.024944035	0.04615151	0.03445747	0.05760316	0.01163879	0.007922516	0.01525413	0.000585938	1.47E-04	0.001025203	0.5664753	0.5556824	0.5772682	3.985812	3.735332	4.196291	0.03886534	0.03183458	0.0458961
68	-9.57E-02	-0.12787038	-0.06345158	-0.12787038	-0.07222731	-0.02486911	0.0470675	0.035581414	0.05855359	0.011883204	0.008005668	0.01576074	0.000612391	1.76E-04	0.001048363	0.5662655	0.5555535	0.5769775	3.972439	3.743687	4.201191	0.03943944	0.03246137	0.0464175
69	-9.43E-02	-0.12756898	-0.06112011	-0.127568098	-0.07058716	-0.02173919	0.04667862	0.03483121	0.05852603	0.011904441	0.007904929	0.01590395	0.00061053	1.61E-04	0.001060216	0.5671231	0.5560741	0.578172	3.944755	3.708808	4.180703	0.0389406	0.03174303	0.04613818
70	-9.31E-02	-0.12969843	-0.0564343	-0.129698843	-0.07241616	-0.018556404	0.04581867	0.032755723	0.05888162	0.011739998	0.007330136	0.01614986	0.000589776	9.39E-05	0.001085584	0.5680846	0.555902	0.5802672	3.925712	3.665556	4.185868	0.03843586	0.03049982	0.04637191
71	-7.64E-02	-0.10774623	-0.04497875	-0.107746723	-0.05451534	-0.00837267	0.04328105	0.032088773	0.05447233	0.011716752	0.00793874	0.01549476	0.000544661	1.20E-04	0.000869443	0.5749121	0.564475	0.5853492	3.722535	3.499654	3.945415	0.03497624	0.02817728	0.0417752
72	-7.84E-02	-0.108249427	-0.04856761	-0.108249427	-0.04968267	-0.005808721	0.04151667	0.030875645	0.0521577	0.011207588	0.007615332	0.01479984	0.000500395	9.65E-05	0.000904291	0.57699	0.567066	0.5869139	3.730886	3.518964	3.942809	0.03392864	0.02746397	0.04039331
73	-9.37E-02	-0.13083504	-0.05662516	-0.130835054	-0.07069843	-0.016144451	0.04697985	0.033748527	0.06021118	0.012009029	0.007632327	0.01656573	0.000628597	1.26E-04	0.001130812	0.567392	0.5550523	0.5797316	3.924099	3.66059	4.187609	0.03872971	0.03069137	0.04676804
74	-9.91E-02	-0.13609450	-0.06212532	-0.136094502	-0.07918844	-0.024811409	0.04934193	0.036013525	0.06253034	0.012242966	0.007790752	0.01669518	0.000657378	1.57E-04	0.001157964	0.5645465	0.5522469	0.5768461	4.027695	3.765041	4.29035	0.04115666	0.0331444	0.04916892
75	-8.81E-02	-0.12526198	-0.05084089	-0.125261918	-0.07371458	-0.019005383	0.0425207	0.02925173	0.05578967	0.010873807	0.006394396	0.01535322	0.000503154	-4.90E-07	0.001006798	0.5677785	0.5554038	0.5801533	3.92275	3.658491	4.187009	0.03679609	0.02873488	0.04485729
76	-8.46E-02	-0.12198678	-0.04717677	-0.121986878	-0.07506537	-0.020070147	0.03899639	0.025658051	0.05233473	0.009941439	0.005438609	0.01444427	0.000418059	-8.82E-05	0.000924336	0.5680904	0.555651	0.5805299	3.943383	3.677743	4.209024	0.03459566	0.02649231	0.04269901
77	-7.51E-02	-0.110189604	-0.04001002	-0.110189604	-0.07581305	-0.024221872	0.03788511	0.025372372	0.05039785	0.009780716	0.005556598	0.01400483	0.000390501	-8.44E-05	0.000865441	0.5672396	0.5555701	0.578909	3.877961	3.628763	4.127159	0.03344353	0.02584175	0.0410453
78	-7.25E-02	-0.107464009	-0.03745412	-0.107464009	-0.07302347	-0.02445704	0.03747722	0.02498074	0.0499557	0.009726016	0.005512112	0.01393992	0.000382784	-9.10E-05	0.000856576	0.5667761	0.5551349	0.5784174	3.853903	3.605308	4.102499	0.03307097	0.02548757	0.04065436
79	-5.04E-02	-0.08536053	-0.01550927	-0.085360563	-0.07534747	-0.023997634	0.03321769	0.020763485	0.04567189	0.009075364	0.004871006	0.01327972	0.000312268	-1.60E-04	0.000784986	0.5655269	0.553912	0.5771418	3.660945	3.412913	3.908978	0.02941213	0.02184592	0.03697835
80	-1.05E-01	-0.1516953	-0.05805544	-0.15169353	-0.08453804	-0.015701786	0.0439394	0.027244103	0.06063469	0.011026245	0.005390157	0.01666233	0.000520261	-1.13E-04	0.001153957	0.5692247	0.5536546	0.5847949	3.979947	3.647451	4.312443	0.03868304	0.02854027	0.04882582
81	-1.15E-01	-0.15877447	-0.07181887	-0.158774487	-0.08304736	-0.0191236 1	0.04727992	0.031876068	0.06288376	0.011697042	0.006463173	0.01693091	0.000572706	-1.58E-05	0.001161178	0.5682606	0.5538016	0.5827196	4.05184	3.743072	4.360607	0.04143398	0.03192504	0.05076292
82	-9.84E-02	-0.14121845	-0.05549323	-0.141218945	-0.07523303	-0.012213397	0.0374415	0.022156951	0.05272606	0.009478759	0.004318916	0.0146386	0.000422563	-1.58E-04	0.000702711	0.5735075	0.557653	0.5826162	3.953108	3.648707	4.257508	0.03536923	0.02068351	0.04465495
83	-9.85E-02	-0.1425522	-0.05446179	-0.1425522	-0.07553181	-0.010773831	0.03558635	0.019880184	0.05129251	0.009005122	0.00370295	0.0143073	0.000385563	-2.11E-04	0.000981714	0.5727191	0.5580714	0.5873668	3.955983	3.643186	4.26878	0.03404849	0.02450663	0.04359034
84	-9.95E-02	-0.14676459	-0.0522256	-0.146764859	-0.07243804	-0.002939317	0.03299556	0.01613959	0.04985153	0.008387307	0.002696977	0.01407764	0.000323204	-3.17E-04	0.000962999	0.5721148	0.5563948	0.5878348	3.916985	3.581289	4.252681	0.03285676	0.02261637	0.04309715
85	-1.02E-01	-0.14410109	-0.05949153	-0.144010109	-0.06843925	-0.005940863	0.03393144	0.018846065	0.04901681	0.008492023	0.003395421	0.01358463	0.000307052	-2.66E-04	0.000879641	0.5753347	0.561226	0.5894034	3.97614	3.675706	4.276573	0.03480084	0.02563613	0.04396555
86	-1.01E-01	-0.14560145	-0.05669488	-0.145601454	-0.0760626	-0.010704639	0.03861517	0.022763489	0.05446686	0.009705252	0.004353954	0.01505655	0.000441721	-1.60E-04	0.001043396	0.5717275	0.5569441	0.5865109	3.972164	3.656469	4.287859	0.03683589	0.02720563	0.04646615
87	-1.04E-01	-0.15181357	-0.05609284	-0.151813857	-0.07771783	-0.007350364	0.03763176	0.020565087	0.05469843	0.009399906	0.003638446	0.01516137	0.000412844	-2.35E-04	0.001060636	0.5712881	0.5553716	0.5872046	3.988072	3.64818	4.327964	0.03615124	0.02578284	0.04651964
88	1.39E-02	-0.04262678	0.07051594	-0.04262678	-0.08335878	-0.000184078	0.04238779	0.022214901	0.06256668	0.01444166	0.007631585	0.02125173	0.0007129	-5.28E-05	0.001478593	0.5578412	0.5390278	0.5766546	2.972666	2.570912	3.374421	0.02783606	0.01558057	0.04009156
89	1.64E-02	-0.02490804	0.05780028	-0.02490804	-0.07188532	-0.01108388	0.04731118	0.032564619	0.06205774	0.01625912	0.011280896	0.02123734	0.000871555	3.12E-04	0.001431283	0.5592978	0.545545	0.5730505	2.940026	2.64834	3.235712	0.02927885	0.02031998	0.03823773
90	1.65E-02	-0.02519424	0.05825568	-0.025194218	-0.07259717	-0.011250571	0.04794515	0.033066373	0.06282393	0.016473141	0.011450281	0.021496	0.000892287	3.28E-04	0.001457034	0.5595453	0.5456693	0.5734214	2.939999	2.64368	3.236318	0.02907077	0.02003157	0.03810997
91	1.93E-02	-0.02281026	0.06146098	-0.022810926	-0.07684623	-0.014895355	0.05078724	0.035761897	0.06581258	0.017516935	0.012444598	0.02258927	0.000990884	4.21E-04	0.001561194	0.5583077	0.544295	0.5723205	2.916783	2.617545	3.216021	0.02939055	0.0202623	0.03851879
92	2.08E-02	-0.020408401	0.06196309	-0.020408401	-0.07977329	-0.019219469	0.05170458	0.037018078	0.06639109	0.017946908	0.012988958	0.02290486	0.0010246	4.67E-04	0.001582049	0.5574771	0.5437804	0.5711739	2.890433	2.597943	3.182923	0.02897782	0.02005543	0.03790021
93	2.24E-02	-0.017101248	0.06188892	-0.017101248	-0.08267606	-0.034607948	0.05557365	0.041490019	0.06965728	0.019357957	0.014603529	0.02411239	0.001154033	6.19E-04	0.001688599	0.555124	0.5418895	0.5682585	2.886311	2.605828	3.166794	0.02759124	0.01903511	0.03614737
94	2.58E-02	-0.013614087	0.06529299	-0.013614087	-0.09329535	-0.03528833	0.05527687	0.041208059	0.06934569	0.019429116	0.014679689	0.02417854	0.001155256	6.21E-04	0.001689259	0.553684	0.5405633	0.5668047	2.867908	2.58772	3.148096	0.02734239	0.01879526	0.03588952
95	2.63E-02	-0.013999851	0.06669013	-0.013999851	-0.09331309	-0.0339954	0.05414295	0.039756249	0.06852964	0.019090894	0.014234154	0.02394763	0.001117196	5.71E-04	0.001663265	0.5534341	0.5400169	0.5668512	2.863682	2.577163	3.150202	0.02701149	0.01827123	0.03575174
96	4.16E-02	0.01234908	0.07082392	0.012349098	-0.09915419	-0.056161523	0.05870366	0.048276371	0.06913094	0.021621465	0.018101366	0.02514156	0.001296061	9.00E-04	0.001691845	0.5372376	0.527513	0.5469622	2.737256	2.529591	2.944922	0.02924249	0.02290767	0.0355773
97	3.89E-02	0.010879423	0.06698629	0.010879423	-0.10369161	-0.062445719	0.0591794	0.049175772	0.06918303	0.021505481	0.018128402	0.02488256	0.0012988	9.19E-04	0.001678503	0.5355399	0.5262104	0.5448693	2.770603	2.571375	2.96983	0.02949077	0.02341333	0.0355682
98	-5.11E-03	-0.01605315	0.00583078	-0.01605315	-0.12907022	-0.112982664	0.06610787	0.062206057	0.07000969	0.02192478	0.020607584	0.02324198	0.001486605	1.34E-03	0.001634704	0.5237889	0.5201501	0.5274278	3.028871	2.951165	3.106578	0.03449957	0.03212913	0.03687001
99	1.65E-02	-0.02597836	0.05901263	-0.025978536	-0.10315491	-0.040675286	0.0587967	0.043643121	0.07395028	0.02017039	0.015054761	0.02528602	0.001239289	6.64E-04	0.001814467	0.5564431	0.5423108	0.5705755	2.920757	2.618965	3.222549	0.02715496	0.01794881	0.03636111
100	1.52E-02	-0.015562468	0.04598509	-0.015562468	-0.09467262	-0.049427109	0.06010463	0.049130948	0.07107831	0.020546881	0.016842326	0.02425144	0.001251017	8.34E-04	0.00166754	0.560458	0.5502239	0.5706922	2.925752	2.707205	3.144299	0.02528112	0.01861435	0.03194788
101	2.20E-02	-0.00636082	0.05026153	-0.006360782	-0.08846364	-0.04683883	0.05888138	0.048785851	0.06897691	0.0203006	0.016892496	0.0237087	0.001207135	8.24E-04	0.001590327	0.5615137	0.5520985	0.5709288	2.902353	2.701295	3.103411	0.02507118	0.01893791	0.03120445
102	2.19E-02	-0.02327905	0.06714752	-0.023279075	-0.08006418	-0.013588793	0.05086965	0.034746955	0.06699235	0.01776801	0.012334013	0.02321959	0.001000934	3.89E-04	0.001612895	0.5576008	0.5425646	0.572637	2.855586	2.534493	3.176678	0.02915877	0.01936386	0.03895369
103	3.20E-02	-0.01644535	0.08039416	-0.016445315	-0.08869101	-0.017501329	0.05295046	0.035684372	0.07021655	0.018704774	0.012875994	0.02453355	0.001090045	4.35E-04	0.001745405	0.5532003	0.5370978	0.5693028	2.798228	2.454364	3.142091	0.03004751	0.01955797	0.04053706
104	1.67E-02	-0.025302598	0.05870423	-0.025302598	-0.07192241	-0.0101664	0.04738458	0.032406496	0.06236266	0.016304532	0.01124815	0.02136091	0.000873642	3.05E-04	0.001442158	0.5592645	0.5452959	0.5732332	2.939814	2.641517	3.238111	0.02960091	0.02056138	0.03876044
105	1.45E-02	-0.029081342	0.05815344	-0.029081342	-0.07154775	-0.007418772	0.04568044	0.030126826	0.06123405	0.01561432	0.010363647	0.02086499	0.000798838	2.08E-04	0.001389199	0.5599516	0.5454461	0.574457	2.953759	2.644001	3.263518	0.02948493	0.02003575	0.03893411
106	8.71E-04	-0.04712492	0.04886667	-0.047124892	-0.07581101	-0.005244653	0.04362112	0.026506211	0.06073603	0.013485668	0.008607924	0.02016341	0.000692661	4.30E-05	0.001342284	0.5594072	0.5434457	0.5753687	3.057491	2.716638	3.398344	0.03084986	0.02045216	0.04124756
107	3.86E-03	-0.044980007	0.052708	-0.044980007	-0.07776872	-0.00595525	0.04385632	0.026438946	0.0612737	0.014474452	0.008594599	0.0203543	0.000696058	3.50E-05	0.001357161	0.5583229	0.5418793	0.5743665	3.037029	2.690152	3.383906	0.03115145	0.02056999	0.04173291
108	2.19E-02	-0.02614946	0.0698679	-0.026149464	-0.06853326	-0.002052065	0.04224886	0.025129351	0.05936837	0.014641652	0.008862355	0.02042095	0.000664894	1.51E-05	0.001314691	0.5627883	0.5468225	0.5787541	2.889983	2.549038	3.230927	0.02746258	0.01706208	0.03786308
109	2.07E-02	-0.02795704	0.069374	-0.027957004	-0.06311902	0.008431999	0.04143164	0.024077917	0.05878537	0.01441697	0.008558605	0.02027534	0.000635053	-2.36E-05	0.00129374	0.565236	0.5490518	0.5814203	2.872232	2.526623	3.217841	0.02694093	0.01639814	0.03748372
110	-1.26E-03	-0.06285216	0.06032349	-0.062852168	-0.06737255	0.023177683	0.03649245	0.014530722	0.05845417	0.012439922	0.005025964	0.01985388	0.000528838	-3.05E-04	0.001362429	0.5683318	0.5478502	0.5888135	2.981248	2.543868	3.418628	0.0273099	0.01396765	0.04065216
111	3.63E-03	-0.063858875	0.07111432	-0.063858875	-0.0678718	0.031351162	0.03576576	0.011706585	0.05983094	0.01237814	0.004254086	0.02050419	0.000500017	-4.04E-04	0.001422447	0.5686901	0.5462468	0.5911335	2.932285	2.453013	3.411556	0.02649025	0.0118701	0.0411104
112	-7.54E-04	-0.06975641	0.06824993	-0.069757641	-0.06125721	0.040156411	0.03989476	0.015288571	0.06450096	0.013979889	0.005673197	0.02228658	0.000671446	-2.63E-04	0.001605412	0.5778736	0.5549257	0.6008216	2.898945	2.408899	3.388992	0.03053187	0.01558304	0.0454807
113	1.58E-03	-0.07353989	0.07670949	-0.07353989	-0.06344292	0.047010041	0.04440533	0.017616473	0.07119419	0.015802299	0.006758769	0.02484583	0.000820395	-1.96E-04	0.001837207	0.5781853	0.5532018	0.6031688	2.856246	2.322731	3.389761	0.03341132	0.01713647	0.04968617

Table S3. continued…

	Body mass			Wing beat frequency			Wing loading			Thorax length (% body length)			Abdomen length (% body length)			Abdomen length (meters)			Inertial power		
Node number	Ancestral state	Upper 95% CI	Lower 95% CI	Ancestral state	Upper 95% CI	Lower 95% CI	Ancestral state	Upper 95% CI	Lower 95% CI	Ancestral state	Upper 95% CI	Lower 95% CI	Ancestral state	Upper 95% CI	Lower 95% CI	Ancestral state	Upper 95% CI	Lower 95% CI	Ancestral state	Upper 95% CI	Lower 95% CI
58	0.8760748	-1.76942793	3.521577	27.37922	10.073798	44.68465	0.08755236	-0.01409863	0.1892034	0.3195407	0.2193811	0.4197003	0.6103145	0.4966009	0.7240282	0.01757996	0.002480124	0.03267979	33.78903	8.468984	59.10908
59	0.9991875	-0.49518934	2.493564	26.45973	16.684342	36.23513	0.08529203	0.02787198	0.14271207	0.3009029	0.2443253	0.3574805	0.6361005	0.5718666	0.7003345	0.01895625	0.010426745	0.02748576	36.44301	22.140364	50.74566
60	0.9535444	-1.35088294	2.257972	27.30315	18.770298	35.83599	0.08795104	0.03782874	0.13807133	0.3037193	0.2543133	0.3531057	0.6346816	0.5786124	0.6907507	0.01873832	0.010730548	0.02566652	36.7972	24.312557	49.28185
61	0.9778323	-0.32071012	2.276375	27.75656	19.262208	36.25091	0.09051374	0.04061845	0.14040902	0.3066549	0.2574916	0.3558181	0.63215	0.5763337	0.6879662	0.01826141	0.010849669	0.02567315	37.19876	24.770435	49.62708
62	1.0435646	-2.26179817	2.348927	27.68571	19.146747	36.22468	0.09398024	0.04382289	0.14413759	0.3072389	0.2578174	0.3566604	0.6316738	0.5755644	0.6877832	0.01867781	0.011227146	0.02681248	38.31992	25.826327	50.81352
63	1.5779134	0.47876808	2.677059	34.27996	27.089959	41.46997	0.15135673	0.10912309	0.19159037	0.2981875	0.2545775	0.3378015	0.6385046	0.5912592	0.68575	0.02352193	0.012428298	0.02979556	48.44294	37.923047	58.96284
64	1.6602942	0.59741823	2.72317	32.29246	25.346668	39.25017	0.14467651	0.11038609	0.18517613	0.2944261	0.2587618	0.3300008	0.643842	0.5985556	0.6895284	0.02364024	0.015059525	0.03255121	51.45612	41.283372	61.6288
65	1.72029	0.80026392	2.640316	30.94837	24.930064	36.96667	0.14110493	0.10575379	0.17645608	0.2906338	0.2558013	0.3254663	0.6479501	0.608404	0.6874963	0.0251024	0.019851129	0.03035366	51.8843	43.078762	60.68986
66	1.8385855	1.02391222	2.653259	30.174	24.844858	35.50315	0.14155014	0.11024708	0.17285321	0.2890027	0.2581589	0.3198465	0.6521146	0.6170969	0.6871323	0.0254423	0.020792357	0.03009224	52.12407	44.326846	59.92129
67	1.8648451	1.1685412	2.612836	29.79839	24.905447	34.69134	0.13941814	0.11067728	0.16815897	0.2876818	0.2593624	0.3160008	0.6550496	0.6228982	0.6872013	0.0257288	0.021258648	0.02979742	51.77322	44.614214	58.93222
68	2.0012356	1.25885109	2.74362	29.50299	24.646715	34.35926	0.14252769	0.11400226	0.17105312	0.2873079	0.259201	0.3154148	0.6564839	0.6245735	0.6883944	0.0259677	0.021730434	0.0302051	52.39662	45.291276	59.50197
69	2.0164672	1.25072931	2.782205	29.51254	24.503502	34.52158	0.14217106	0.11274829	0.17159383	0.2877666	0.2587755	0.3167577	0.6563529	0.6234386	0.6892671	0.0256254	0.021254508	0.02999577	51.8438	44.514936	59.17266
70	1.9132331	1.06893064	2.757536	29.72171	24.198745	35.24467	0.14048241	0.10804087	0.17292394	0.2851196	0.253154	0.3170852	0.6599139	0.6236226	0.6962052	0.0254212 5	0.020602192	0.03042031	51.7266	43.08082	59.24242
71	1.6977903	0.92446042	2.42112	30.97813	26.246605	35.70976	0.15337497	0.12595669	0.18154329	0.2908752	0.2624897	0.3182607	0.6637025	0.6327011	0.6948838	0.0233114	0.019202567	0.02745972	46.32448	39.401505	53.24745
72	1.6168828	0.92911735	2.304648	32.15003	27.651045	36.64901	0.15817612	0.13174937	0.18460287	0.2930688	0.2670298	0.3191078	0.6605388	0.630976	0.6901015	0.02252305	0.018597463	0.02644863	44.85896	38.276368	51.44154
73	2.1413467	1.28616156	2.996532	29.31742	23.723268	34.91157	0.13434577	0.11048608	0.17620547	0.2910662	0.2586886	0.3234438	0.6526101	0.6158511	0.6893692	0.02533773	0.020456559	0.0302189	51.73266	43.547706	59.91762
74	2.1930682	1.34065705	3.045479	29.01875	23.442743	34.59475	0.14803881	0.11528571	0.18079192	0.2859735	0.253701	0.3182461	0.658972	0.6223322	0.6956118	0.0272194 1	0.022354075	0.03208475	54.27935	46.120943	62.43776
75	1.4593551	0.60173694	2.316973	29.88732	24.272749	35.49738	0.12341105	0.09045787	0.15636423	0.2859669	0.2532294	0.3181688	0.6537	0.6205063	0.6942336	0.0262301	0.019327949	0.02918807	48.75376	40.545519	56.96201
76	1.073758	0.21165613	1.93586	30.34736	24.707962	35.98676	0.10723592	0.07411046	0.14036139	0.2838644	0.2512249	0.3165038	0.6583879	0.6213315	0.6954443	0.0227869	0.017866254	0.02770756	46.37297	38.12181	54.62413
77	0.9177243	0.10898399	1.726465	30.18267	24.89233	35.473	0.10175211	0.07067702	0.13827221	0.2870583	0.2564392	0.3176775	0.6542085	0.6194458	0.6889712	0.0218838 2	0.017267204	0.02649936	45.47001	37.729571	53.21044
78	0.8863261	0.29954134	1.693111	30.22035	24.942808	35.49789	0.10071342	0.07073146	0.13713137	0.2875017	0.2569566	0.3180469	0.6536266	0.618948	0.6883035	0.0216182	0.017013403	0.02623323	44.99099	37.269268	52.71271
79	0.6062672	-0.19868985	1.411224	30.71075	25.445159	35.97633	0.08509818	0.05416845	0.1160279	0.2872328	0.2567569	0.3177088	0.6532436	0.6186435	0.6878437	0.0192514	0.014620656	0.02380962	41.33386	33.629631	49.03808
80	1.4984541	0.41938106	2.577527	30.92465	23.865946	37.98335	0.13441025	0.09294787	0.17587263	0.2890533	0.2481992	0.3299073	0.6432212	0.5968385	0.6896038	0.0249186 7	0.018759603	0.03107773	51.90785	41.580064	62.23563
81	1.6435768	0.64151177	2.645642	29.2888	22.733837	35.84376	0.13753765	0.09903423	0.17604107	0.2934888	0.2555503	0.3314273	0.6367814	0.5937088	0.6798539	0.0263398 3	0.020620305	0.03205935	56.26853	46.677787	65.85927
82	1.5617835	0.57387131	2.549656	41.79636	35.334116	48.25861	0.18956577	0.15166094	0.22752461	0.2965654	0.2692121	0.3339659	0.6272763	0.58483 1	0.6697394	0.0293064	0.027620909	0.0306927	44.40023	34.945137	53.85532
83	1.430576	0.41543371	2.445718	43.45362	36.813116	50.09412	0.18967785	0.15067196	0.22868375	0.2952772	0.2568436	0.3337108	0.6263643	0.5827296	0.6699989	0.0251733 3	0.015723169	0.0273115	43.0497	33.333796	52